



HAL
open science

SN 2018hna: Adding a piece to the puzzles of the explosion of blue supergiants

Danfeng Xiang, Xiaofeng Wang, Xinghan Zhang, Hanna Sai, Jujia Zhang, Thomas Brink, Alexei Filippenko, Jun Mo, Tianmeng Zhang, Zhihao Chen, et al.

► To cite this version:

Danfeng Xiang, Xiaofeng Wang, Xinghan Zhang, Hanna Sai, Jujia Zhang, et al.. SN 2018hna: Adding a piece to the puzzles of the explosion of blue supergiants. Monthly Notices of the Royal Astronomical Society, 2023, 520 (2), pp.2965-2982. 10.1093/mnras/stad340 . hal-04244781

HAL Id: hal-04244781

<https://cnrs.hal.science/hal-04244781v1>

Submitted on 3 Jan 2024

HAL is a multi-disciplinary open access archive for the deposit and dissemination of scientific research documents, whether they are published or not. The documents may come from teaching and research institutions in France or abroad, or from public or private research centers.

L'archive ouverte pluridisciplinaire **HAL**, est destinée au dépôt et à la diffusion de documents scientifiques de niveau recherche, publiés ou non, émanant des établissements d'enseignement et de recherche français ou étrangers, des laboratoires publics ou privés.



Distributed under a Creative Commons Attribution 4.0 International License

SN 2018hna: Adding a piece to the puzzles of the explosion of blue supergiants

Danfeng Xiang¹,^{*} Xiaofeng Wang,^{1,2,3} Xinghan Zhang,¹ Hanna Sai,¹ Jujia Zhang^{1,4},
 Thomas G. Brink,⁵ Alexei V. Filippenko,⁵ Jun Mo,¹ Tianmeng Zhang,^{6,7} Zhihao Chen,¹ Luc Dessart,⁸
 Zhitong Li,^{7,9} Shengyu Yan,¹ Sergei I. Blinnikov,^{10,11} Liming Rui,¹ E. Baron¹² and J. M. DerKacy^{12,13}

¹Department of Physics and Tsinghua Center for Astrophysics (THCA), Tsinghua University, Haidian District, Beijing 100084, China

²Beijing Planetarium, Beijing Academy of Sciences and Technology, Beijing 100044, China

³Purple Mountain Observatory, Chinese Academy of Sciences, Nanjing 210023, China

⁴Yunnan Observatories, Chinese Academy of Sciences, Kunming 650216, China

⁵Department of Astronomy, University of California, Berkeley, CA 94720-3411, USA

⁶Key Laboratory of Space Astronomy and Technology, National Astronomical Observatories, Chinese Academy of Sciences, Beijing 100101, China

⁷School of Astronomy and Space Science, University of Chinese Academy of Sciences, Beijing 101408, China

⁸Institut d'Astrophysique de Paris, CNRS-Sorbonne Université, 98 bis boulevard Arago, F-75014 Paris, France

⁹Key Laboratory of Optical Astronomy, National Astronomical Observatories, Chinese Academy of Sciences, Beijing 100101, China

¹⁰National Research Center 'Kurchatov Institute', 123182 Moscow, Russia

¹¹Kavli IPMU (WPI), UTIAS, The University of Tokyo, Kashiwa, Chiba 277-8583, Japan

¹²Homer L. Dodge Department of Physics and Astronomy, University of Oklahoma, 440 W. Brooks, Norman, OK 73019-2061, USA

¹³Department of Physics, Virginia Tech, 850 West Campus Drive, Blacksburg, VA 24061, USA

Accepted 2023 January 20. Received 2023 January 10; in original form 2022 November 8

ABSTRACT

We present extensive optical/ultraviolet observations and modelling analysis for the nearby SN 1987A-like peculiar Type II supernova (SN) 2018hna. Both photometry and spectroscopy covered phases extending to >500 d after the explosion, making it one of the best-observed SN II of this subtype. SN 2018hna is obviously bluer than SN 1987A during the photospheric phase, suggesting higher photospheric temperature, which may account for weaker Ba II $\lambda 6142$ lines in its spectra. Analysis of early-time temperature evolution suggests a radius of $\sim 45 R_{\odot}$ for the progenitor of SN 2018hna, consistent with a blue supergiant (BSG). By fitting the bolometric light curve with hydrodynamical models, we find that SN 2018hna has an ejecta mass of $\sim (13.7\text{--}17.7) M_{\odot}$, a kinetic energy of $\sim (1.0\text{--}1.2) \times 10^{51}$ erg, and a ^{56}Ni mass of about $0.05 M_{\odot}$. Moreover, based on standard stellar evolution and the oxygen mass ($0.44\text{--}0.73 M_{\odot}$) deduced from nebular [O I] lines, the progenitor of SN 2018hna is expected to have an initial main-sequence mass $< 16 M_{\odot}$. In principle, such a relatively low-mass star cannot end as a BSG just before core-collapse, except some unique mechanisms are involved, such as rapid rotation, restricted semiconvection, etc. On the other hand, binary scenario may be more favourable, like in the case of SN 1987A. While the much lower oxygen mass inferred for SN 2018hna may imply that its progenitor system also had much lower initial masses than that of SN 1987A.

Key words: supernovae: individual: SN 1987A – supernovae: individual: SN 2018hna.

1 INTRODUCTION

Stars in the Universe may end their lives in different ways after experiencing long-term evolution, and they will eventually ‘die’ in silence or spectacular explosions. Core-collapse supernovae (SNe) are the violent deaths of massive stars that have initial masses $\gtrsim 8 M_{\odot}$. Some of these stars keep most of their hydrogen envelopes prior to explosion, so the spectra of these SNe show strong hydrogen lines with P Cygni profiles. These H-rich SNe are classified as SNe II, while H-poor ones are classified as SNe I (e.g. Filippenko 1997). The progenitors of SNe II are believed to be red supergiants (RSGs) with large low-density hydrogen envelopes. Unlike H-poor SNe (SNe Ia

and Ibc), recombination of H in the ejecta plays an important role during the photospheric phase of SNe II.

At the beginning of the explosion, the shock breaks out from the stellar surface, and then the shocked envelope cools down by emitting light in ultraviolet (UV) and optical bands. During this very early phase, the light curves rise to a peak quickly, usually in a few days. Since the temperature of the H-rich ejecta is high, almost all H atoms are ionized at early phases. As time goes by, the expanding ejecta cool down and the H^+ ions start to recombine with electrons to form neutral H, releasing photons. According to theoretical analysis, during the recombination phase the photospheric temperature is roughly the H-recombination temperature (~ 5500 K), and the size of the photosphere remains almost constant. As a result, the SN luminosity remains unchanged for ~ 100 d, and this period is called a ‘plateau’ in light curves of SN IIP. Some other H-rich SNe do not have plateaus; their light curves decline linearly (in magnitudes)

* E-mail: xiangdf@mail.tsinghua.edu.cn (DX);

wang_xf@mail.tsinghua.edu.cn (XW)

and thus are called Type IIL. It has been confirmed that the progenitor stars of SNe IIP are consistent with red supergiants (RSGs; see the review by Smartt 2015).

While most H-rich SNe can be classified as Type IIP or IIL (but see Anderson et al. 2014 and the review by Gal-Yam 2017 for arguments for a continuous distribution of SNe II), there are some other peculiar subtypes that show different properties. The most well-known one is the SN 1987A-like subtype, named after its prototype SN 1987A, which exploded in the Large Magellanic Cloud (LMC) and was the closest SN discovered over the past few centuries. Extensive and detailed observations of SN 1987A show that it had the spectral characteristics of SNe II (i.e. the persistent H lines), but it took more than 80 d to reach its primary light-curve peak after a short and rapid rise (Catchpole et al. 1987, 1988; Menzies et al. 1987; Suntzeff et al. 1988; Whitelock et al. 1988; Pun et al. 1995). There is no plateau in the light curves of SN 1987A-like SNe II (hereafter ‘87A-like SNe’); instead, they rise to their peaks slowly. After a rise of ~ 80 d, these SNe start to decline rapidly, followed by a linear decay which also appears in SNe IIP/IIL. It is now clear that the distinctive behaviour of 87A-like SN light curves is the result of smaller, denser, and hotter progenitors – blue supergiants (BSGs). In comparison with RSGs, the envelopes of BSGs have steeper density profiles and are nonconvective. Some studies also show that 87A-like SNe ejected more mass and synthesized more ^{56}Ni in the explosion (Taddia et al. 2016), which can explain the peculiar light-curve evolution of this subclass.

Moreover, the spectra of 87A-like SNe show prominent Ba II absorption lines in addition to features typically seen in typical SNe II (Mazzali & Chugai 1995). Ba II lines also appear in normal SNe II, but later (>40 d), and they tend to emerge in dimmer events (Gutiérrez et al. 2017). There remains the issue of why SN 1987A displayed stronger Ba II lines than other SNe II, but the enhanced He and *s*-process elements in the circumstellar material suggested that these apparent enhancements are caused by real abundance effects (Hoeflich 1988; Mazzali, Lucy & Butler 1992). Recent studies have made some attempts to interpret the spectral signatures of peculiar SNe II (e.g. Dessart & Hillier 2005, 2008, 2010; Dessart, Hillier & Wilk 2018; Dessart & Hillier 2019). The connection of *s*-process, He burning, and binary interaction can probably shed light on this issue.

SN 1987A was well studied in many aspects, including the analysis of its pre-explosion star. The progenitor of SN 1987A, Sk $-69^{\circ}202$, was identified as a compact BSG with radius $R \approx 45 R_{\odot}$ and temperature $T_{\text{eff}} \approx 16\,000$ K (Woosley, Pinto & Ensmann 1988). While stellar-evolution theory predicts that massive stars with initial masses lower than $30 M_{\odot}$ explode at the RSG stage ($R > 100 R_{\odot}$), SN 1987A was an exception. New hypotheses were proposed to explain BSGs as progenitors of H-rich SNe, such as low metallicity, new treatment of convection, dredge-up of He layers, rapid rotation, binary interaction, and star mergers (see the review by Podsiadlowski 1992). Furthermore, the triple-ring structure around SN 1987A found by Wampler et al. (1990) imposes additional constraints on the evolution of the precursor, favouring a binary evolution scenario, in which the progenitor of SN 1987A first evolved to RSG phase and then went blue again after obtaining matter from the companion by either accretion or merging. Nevertheless, the evolutionary mechanism of the progenitors of other 87A-like SNe remains unclear.

Thus far, only a few well-observed SNe II have been identified as 87A-like objects: SN 1998A (Pastorello et al. 2005), SN 2006au, and SN 2006V (Taddia et al. 2012), SN 2009E (Pastorello et al. 2012a), and recently SN 2018hna (Singh et al. 2019). Other samples are presented by Kleiser et al. (2011), Taddia et al. (2016), Takáts

et al. (2016), and Kelly et al. (2016). All of the above SNe have long rise times and H-rich spectra. Among this sample, SN 2018hna is the best observed after SN 1987A. This peculiar SN II exploded in a nearby irregular galaxy UGC 7534, and it was discovered by Koichi Itagaki on 22.82 October 2018¹ (MJD 58413.82; UT dates are used throughout this paper). Singh et al. (2019) studied the observed properties of SN 2018hna, suggesting that it had a progenitor with an initial mass of $14\text{--}20 M_{\odot}$, and an ejected ^{56}Ni mass of $\sim 0.087 M_{\odot}$ according to their hydrodynamical modelling of the multiband light curves. Polarimetric observations of SN 2018hna were published by Maund et al. (2021) and Tinyanont et al. (2021) in optical and near-infrared (NIR) bands, respectively. SN 2018hna showed significant polarization in the NIR bands at 182 d, with a typical value of $p \approx 2$ per cent, but dust formation was not responsible for this large polarization. In the optical, it had $p < 1$ per cent in RINGO3 b^* and g^* bands before $t \approx 115$ d and 1.29 per cent in r^* at day 102. By comparing with SN 1987A, Tinyanont et al. (2021) concluded that the polarization behaviour of SN 2018hna is similar to that of SN 1987A, so their ejecta share a similar underlying geometry observed at a similar inclination angle.

In this paper, we present extensive optical (and UV) observations SN 2018hna, including light curves and spectra covering pre-maximum times to very late nebular phases. These data sets are used to constrain the explosion parameters and determine the properties of the progenitor star. Furthermore, along with SN 2018hna, we collect some well-observed 87A-like SNe in history, to discuss the common characteristics of this particular family and the differences among the individuals. The paper is structured as follows. Our photometric and spectroscopic observations are presented in Section 2. Then, in Section 3, we discuss the properties of the multiband and bolometric light curves of SN 2018hna compared to other 87A-like SNe, followed by comparisons of spectral features in Section 4. Next, in Section 5, we estimate and analyse the explosion parameters using both semi-analytical and hydrodynamic methods. In Section 6, we explore the properties and possible evolutionary pathways of the progenitor star of SN 2018hna through the characteristics of its nebula phase spectra. Finally, we summarize our conclusions in Section 7.

2 DATA

Our photometric and spectroscopic observations of SN 2018hna were obtained by ground-based instruments, including the 80-cm Tsinghua-NAOC Telescope at Xinglong Observatory (hereafter TNT; Wang et al. 2008; Huang et al. 2012), the 2.4-m telescope at Lijiang Observatory (hereafter LJT), the 2.16-m telescope at Xinglong Observatory (hereafter XLT), the ARC 3.5-m telescope at Apache Point Observatory (hereafter ARC), and the 10-m Keck-I telescope on Maunakea, Hawai‘i. The Zwicky Transient Facility (ZTF; Bellm et al. 2019) Bright Transient Survey (BTS; Perley et al. 2020) monitored SN 2018hna in the *gr*-bands until very late phases, and the data are publicly available (ZTF ID: ZTF18acbwaxk).² We also include early-time UV-optical photometry obtained by the Ultraviolet/Optical Telescope (UVOT; Gehrels et al. 2004; Roming et al. 2005) onboard the *Neil Gehrels Swift Observatory* (Gehrels et al. 2004). Details of these observations are presented below.

¹<https://www.wis-tns.org/object/2018hna>

²lasair.roe.ac.uk/object/ZTF18acbwaxk/

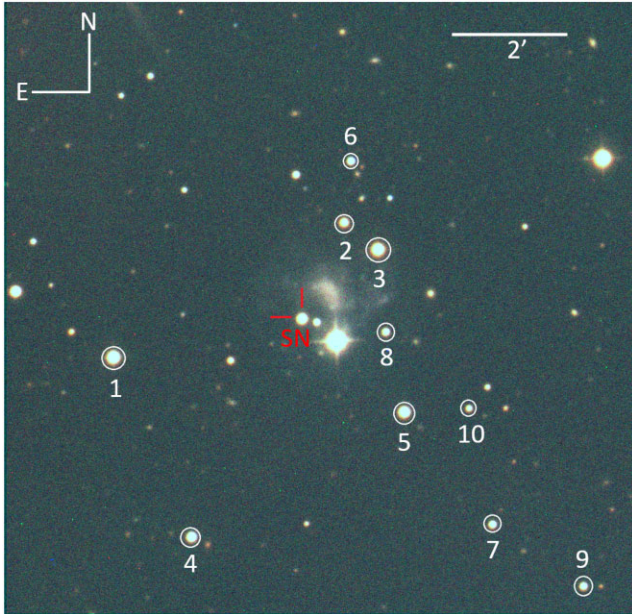


Figure 1. Pseudo-colour finder chart of SN 2018hna and its host galaxy UGC 7534 produced from the BVr -band images obtained by the Tsinghua-NAOC 0.8-m telescope on 2018, January 4. The SN is located southeast of the centre of UGC 7534. The reference stars used for flux calibration are marked by white circles. North is up and east is left.

2.1 Optical photometry

Photometric observations by TNT spanned the phases from 2018 December 4 to 2019 March 3, lasting for over 200 d with an average cadence of <4 d. The filters used by TNT were the generic Johnson BV and Sloan gri bands. The reference images were obtained in all corresponding bands after the SN faded away.

All of the $BVgri$ images are preprocessed using standard IRAF³ routines, which includes corrections for bias, flat field, and removal of cosmic rays. To remove contamination from the host galaxy, we applied a template-subtraction technique based on the *hotpants* package.⁴ For SN 2018hna and the reference stars, the instrumental magnitudes were measured using standard-point-spread-function (PSF) photometry. These were then converted to standard Johnson BV and Sloan gri magnitudes using the zero-points and colour terms of the filters, which are obtained by comparing the instrumental and standard magnitudes of the reference stars in field of the SN (see Fig. 1). Standard magnitudes of the reference stars in BV -bands are obtained from the AAVSO Photometric All-Sky Survey (APASS),⁵ and magnitudes in gri -bands are obtained from the Sloan Digital Sky Survey (SDSS; Ivezić et al. 2007). Photometric results of the reference stars and SN 2018hna are listed in Appendix C.

Our light curves together with the public ZTF and UVOT data are shown in Fig. 2. Light curves from different sources agree well with each other, except for the UVOT uvb and TNT B observations in the postmaximum phases. We notice these differences and evaluate that they have no impact on our analysis. We also made comparisons with

light curves from Singh et al. (2019) and found consistency of both data sets. We include complementary data from Singh et al. (2019) when necessary.

2.2 Optical spectroscopy

A sequence of optical spectra was obtained by the 2.16-m telescope at Xinglong Observatory of NAOC, the 2.4-m telescope at Lijiang Observatory, and the 3.5-m telescope at Apache Point Observatory. A late-time spectrum was taken by the 10-m Keck-I telescope with the Low-Resolution Imaging Spectrometer (LRIS; Oke et al. 1995) on 2020 March 24. The spectroscopy of Keck-I used a slit with width of 1.0 arcsec and the slit was placed along the parallactic angle. The resultant spectrum has a resolution of $\sim 4 \text{ \AA}$ in the blue side ($<5600 \text{ \AA}$) and $\sim 6.9 \text{ \AA}$ in the red side ($>5600 \text{ \AA}$). All our spectra cover the phases from ~ 46 to 522 d after the explosion of SN 2018hna. Three pieces of optical spectra are available on the Transient Name Server (TNS). Details of the TNS spectra are listed in Table C4. Observation details are listed in Table C5 and the entire spectral sequence is displayed in Fig. 3.

The spectral evolution of SN 2018hna is characterized by typical features of SNe II, showing strong P Cygni lines of the hydrogen Balmer series as well as absorption lines of Fe II, Na I, Ca II, Sc II, and Ba II. In the nebular phase, the spectra are dominated by emission lines of H, Na I, and Ca II, along with forbidden lines of [Fe II], [Ca II], and [O I]; all of these are commonly seen in late-time spectra of SNe II.

2.3 Distance and extinction

The host galaxy of SN 2018hna, UGC 7534, is an irregular dwarf galaxy, which was classified as an IBm-type galaxy according to the third reference catalogue of bright galaxies (RC3.9, de Vaucouleurs et al. 1991). The metallicity of UGC 7534 was found to be subsolar ($Z \sim 0.3 Z_{\odot}$, Singh et al. 2019). The heliocentric velocity of UGC 7534 gives a redshift of 0.002408 (Falco et al. 1999). The distance to this galaxy was estimated to be 10.50 Mpc through the Tully–Fisher relation (Karachentsev, Makarov & Kaisina 2013). Given a measurement error of 25 per cent (Karachentsev et al. 2013), we apply a distance of 10.50 ± 2.63 Mpc, and a distance modulus of $\mu = 30.11 \pm 0.54$ mag.

Since there is no significant Na I D absorption in optical spectra of SN 2018hna at the redshift of the host, we adopt a Galactic reddening of $E(B - V) = 0.01$ mag (Schlafly & Finkbeiner 2011) and neglect extinction in the host galaxy. Following Singh et al. (2019), we adopt the first-light date as MJD = 58411 in this paper.

3 LIGHT CURVES AND COLOUR EVOLUTION

In this section, we compare the multiband light curves and colour evolution of SN 2018hna to other 87A-like SNe. As shown in Fig. 2, the light curves of SN 2018hna are similar to those of typical 87A-like SNe II, showing a long rise to peak. Light curves in the UV and B bands exhibit early bumps before rising to the main peaks, which is due to cooling of the shocked H-rich envelope, common in SNe II. Then the light curves rise slowly to peaks at ~ 80 d after explosion, followed by a rapid decline in ~ 30 d. After that, the light curves decline linearly with a rate of $\sim 1 \text{ mag } (100 \text{ d})^{-1}$ in all optical bands except in r , where a slower decline is observed before ~ 250 d and a faster decline is seen after that. This phenomenon is also observed in SN 1987A, and is most likely due to the emission of hydrogen, as the transmission curve of the r -band filter peaks near the wavelength

³IRAF is distributed by the National Optical Astronomy Observatories, which are operated by the Association of Universities for Research in Astronomy, Inc., under cooperative agreement with the National Science Foundation (NSF).

⁴<https://github.com/acbecker/hotpants>

⁵www.aavso.org/apass

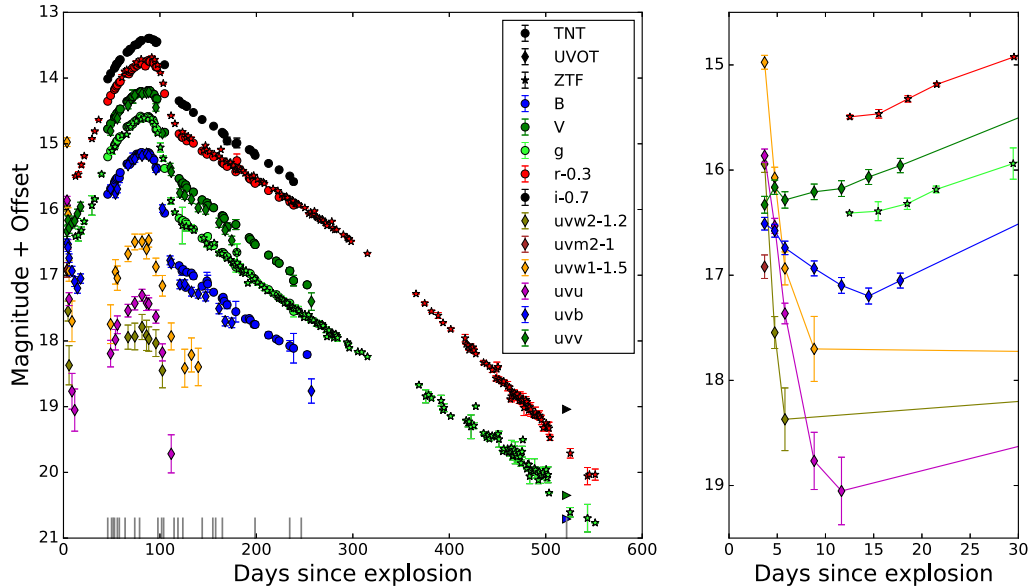


Figure 2. UV-optical light curves of SN 2018hna. The grey ticks at the bottom mark the epochs of spectroscopic observations. Magnitudes in BVi bands inferred from the Keck spectrum at day 522 are presented by the coloured triangles. The right-hand panel shows a close-up view of the early phases.

of $H\alpha$. We use the Keck-I spectrum and the observed magnitudes in g and r as flux calibrators to determine the Bvi magnitudes on day 522.

In Fig. 4, we compare the BVR light curves of SN 2018hna with those of other 87A-like SNe. The peak absolute magnitudes of SN 2018hna in these bands are fainter than the bright SN 2006V and SN 2006au, but comparable to SN 1987A and SN 2009mw. In B -band, although SN 2018hna is similar to SN 1987A around the peak, its shock-cooling-phase emission and the radioactive tail are much fainter than those of the latter, while in V -band it is fainter than SN 1987A at all phases. In r -band, the overall light-curve evolution of SN 2018hna becomes quite similar to that of SN 2009E and SN 2009mw, although SN 2009E shows an early-time bump.

The colour evolution of SN 2018hna, compared with other 87A-like SNe is shown in Fig. 5. The $V - R$ colours of SNe are transformed to $g - r$ using the conversion formula from table 3 of Jordi, Grebel & Ammon (2006). The $B - V$ colour curves of 87A-like SNe all show two peaks. They share similar evolution before reaching the first peak, although the first-peak time varies. One can see that the earlier the first peak occurs, the shorter duration it takes the colour curves to turn red again. This might be also related to the luminosities of the SNe. For example, the most luminous SN 2006V and SN 2006au have a faster turn-off time, while the remaining relatively faint events like SNe 1987A, 2009E, and 2018hna show slower colour-turn even though their colour differences can be as large as 0.5 mag. Since the early $B - V$ colours are tied to the photospheric temperature, the correlation of colour evolution with peak luminosity may be a result of different progenitor properties such as stellar radius and the temperature of the shocked envelope. Among the slow events, SN 1987A shows unique behaviour in $B - V$: it is slightly brighter than SN 2018hna but its $B - V$ turn is slower than that of all others. This might imply that the specific shock energy (i.e. $\sim E/M$) in SN 1987A is lower than in other objects, which can also be confirmed by its low expansion velocities (see Fig. 7). After the second peak, the $B - V$ colours of SN 2018hna and all comparison SNe II exhibit similar linear declines. The dispersion of $B - V$ colour evolution reaches a minimum at ~ 100 d, at which time recombination

ends and all SNe share a similar effective temperature. After that, SN 2018hna enters the fast-declining phase. At $t \approx 100$ d, the $V - R$ and $g - r$ colours of different 87A-like SNe also tend to become more consistent, and they reach the reddest peak values at much later phase ($t \approx 300$ d). After that, both the $V - R$ and $g - r$ colours evolve blueward in a linear fashion.

4 SPECTROSCOPIC EVOLUTION

As shown in Fig. 3, the spectral evolution of SN 2018hna is similar to that of a typical SN II, and we do not detect any significant narrow emission lines which probe interaction (e.g. Chugai 2001). In the photospheric phase, the spectra are dominated by Balmer lines with P Cygni profiles, along with absorption lines of Na I D, Fe II, Ca II, Sc II, and the characteristic Ba II lines of 87A-like SNe. At later phases, H absorption lines vanish as the ejecta expand and become geometrically diluted, and forbidden lines of [O I] and [Ca II] emerge. Below we discuss the spectral properties of SN 2018hna, such as line velocities, line strength, in comparison with other 87A-like SNe II.

4.1 Line velocities

We measured the expansion velocities of several absorption lines, as shown in Fig. 6. The line velocities are measured from the blueshifted minima of the corresponding absorption troughs. Spectral data from Singh et al. (2019) are also included in our analysis. Note that the velocity inferred from Na I D absorption shows a steep rise at ~ 105 d, probably a measurement artefact since the absorption can be contaminated by other species such as He I. In Fig. 7, the velocity of Fe II $\lambda 5169$, which is often used to trace the SN photosphere, is measured for SN 2018hna and compared with those of several 87A-type objects. As it can be seen, the 87A-like SNe II show a large diversity in Fe II velocity, with SN 2018hna lying between SN 1987A and SN 1998A but close to SN 2006V. No strong correlation seems to exist between the expansion velocity and peak luminosity for this peculiar subgroup of SNe II when inspecting the light curves shown in Fig. 4, although this correlation has been proposed for normal

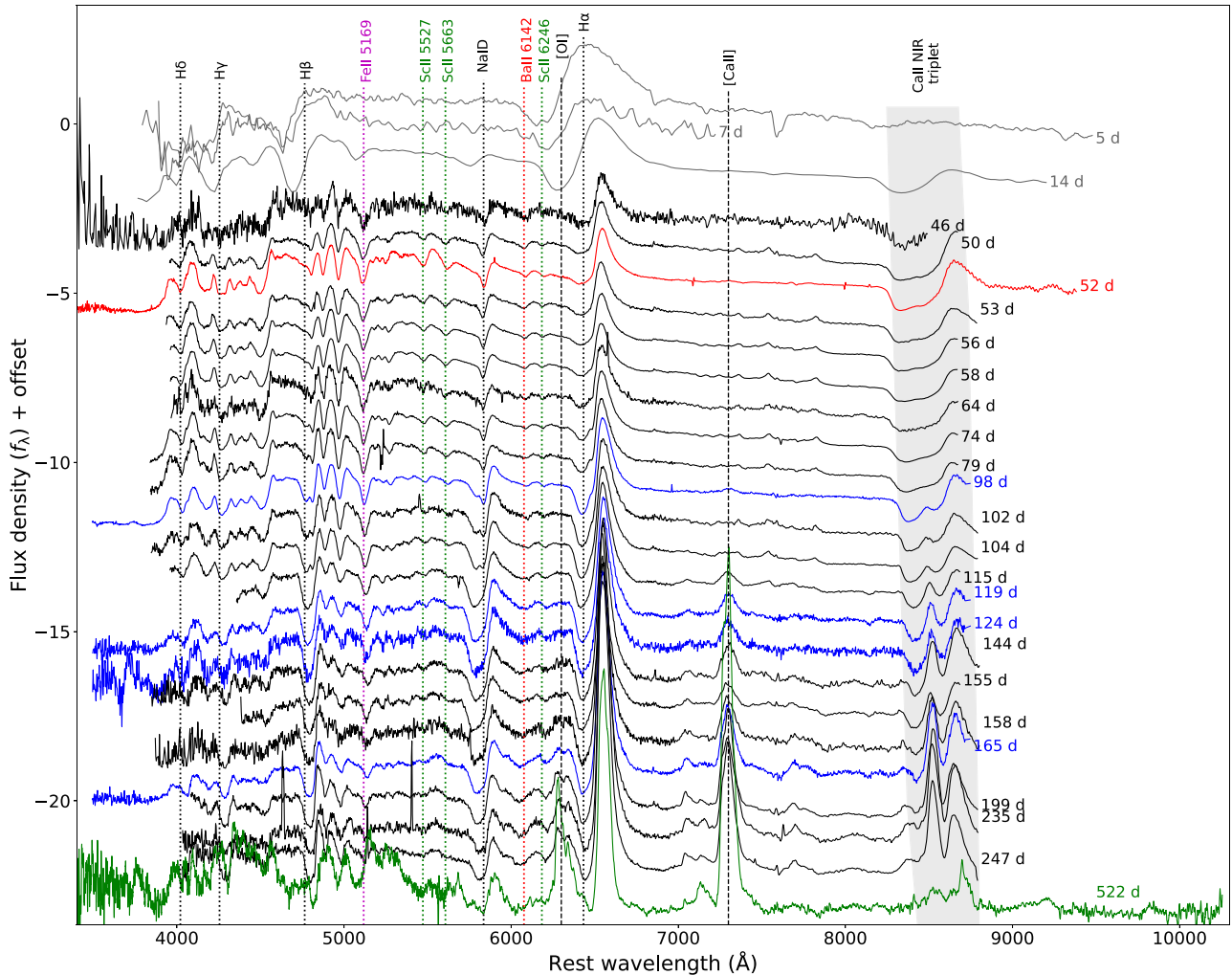


Figure 3. Spectral sequence of SN 2018hna. Different colours represent different instruments: black-XLT, red-ARC, blue-LJT, green-Keck-I, grey-TNS. Numbers to the right of each spectrum display phases since explosion (MJD 58411). The dominant spectral features are marked by dotted vertical lines.

SNe IIP (e.g. Hamuy & Pinto 2002). Among our comparison sample, SN 2006au and SN 2006V have comparable peak luminosities, while their velocities could differ by $\sim 1500 \text{ km s}^{-1}$.

4.2 Spectral evolution

Fig. 8 shows the spectral evolution of SN 2018hna during the photospheric phase, together with that of the comparison sample of 87A-like SNe II. SN 2018hna is found to show close resemblances to SN 2006V, except that the latter has slightly narrower line profiles. Compared to SN 1987A, the metal lines such as Na I, Sc II, Fe II, and the characteristic Ba II are quite weak in SN 2018hna, SN 2006V, and SN 2006au at photospheric phase. Note that SN 1998A has metal lines with strength lying between the above three SNe and SN 1987A. In the spectra of 87A-like SNe, the strength of Ba II lines is generally proportional to that of other metal lines; while SN 2009E is an exception, which has weak metal lines as SN 2018hna, but it shows stronger Ba II $\lambda 6142$. This indicates that, in addition to metal abundance, there are other factors that may affect the formation of Ba II absorption feature. To figure out the possible factors affecting the intensity of spectral lines in SN spectra, we try to compare observations with theoretical models.

Dessart & Hillier (2019) computed a set of non-local thermodynamic equilibrium (NLTE) time-dependent radiative transfer models based on the explosion of a BSG, which originally evolved from a star having an initial mass of $15 M_{\odot}$ and extremely low metallicity and subsequently exploded with a thermal bomb. Strong mixing is imposed, which erases the original low metallicity of the progenitor (i.e. the metal-rich inner layers pollute the outer H-rich layers). These models are characterized with a set of different initial conditions such as ejecta mass, kinetic energy, ^{56}Ni mass and element abundance. We caution that the models of Dessart & Hillier (2019), which are based on limited ejecta parameters, are not expected to match all of the observational properties. But comparing the spectra of SN 2018hna with those predicted by models can give a clue on how different physical conditions can influence the spectra. As an example, we perform a detailed analysis with one of these models below.

Model a4 from Dessart & Hillier (2019) has an ejecta mass of $13.22 M_{\odot}$, a kinetic energy of 1.26×10^{51} erg, a ^{56}Ni mass of $0.084 M_{\odot}$, and a mixing length of $4 M_{\odot}$. Comparison of the spectra of SN 2018hna with model a4 is shown in Fig. 9. In the early phases (i.e. at $t < 30$ d), model a4 has similar line velocities but weaker Ba II and Fe II lines in comparison with the observations. Subsequently, Ba II lines in the models become stronger than the observations, but

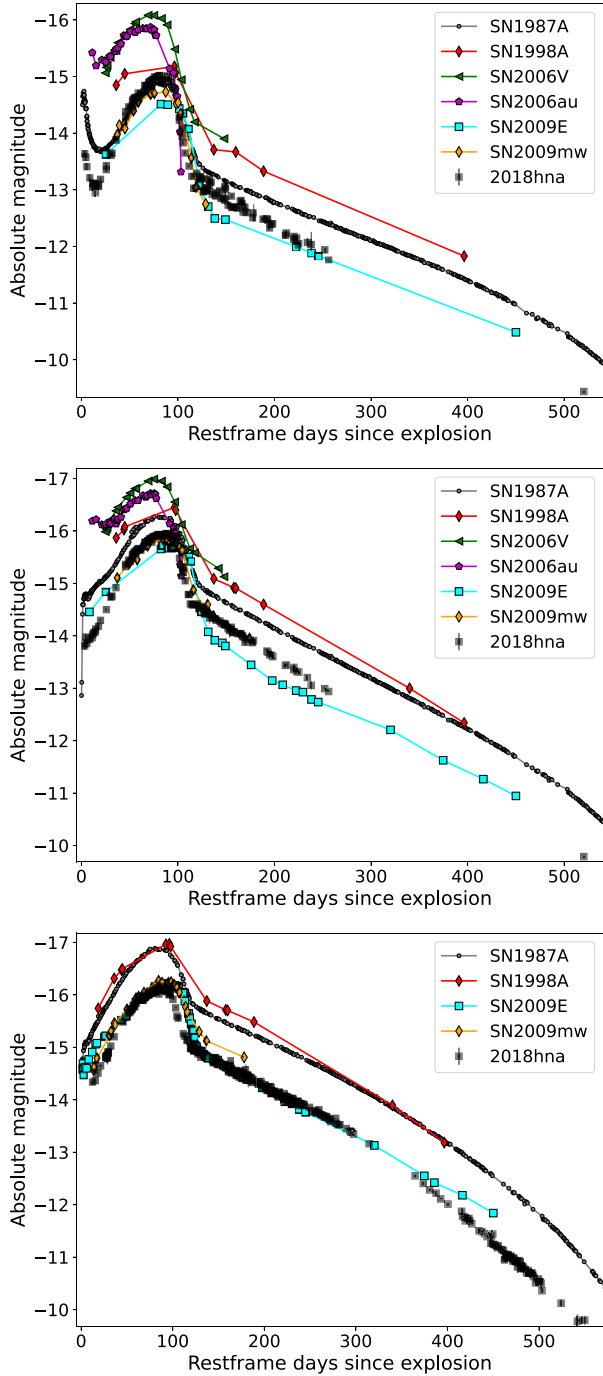


Figure 4. Light curves of SN 2018hna compared with those of other 87A-like SNe in *B* (top), *V* (middle), and *r* (bottom). The *R*-band light curve of SN 1987A is plotted instead of *r*.

other metal lines are still weaker until day 119. The metal lines match better with the observations in model a4ni (with enhanced ^{56}Ni by a factor of ~ 1.5 compared to model a4), despite that they have weak Ca emission after transition to the nebular phase; less amount of ^{56}Ni might reduce the difference. Since the models have strong mixing thus high metal abundance in the ejecta, the weak metal lines in SN 2018hna are likely due to lower metallicity in the ejecta, hence smaller mixing length in the model.

Discrepancy between the models and observations are large at intermediate phases (30–110 d after the explosion), diminishing

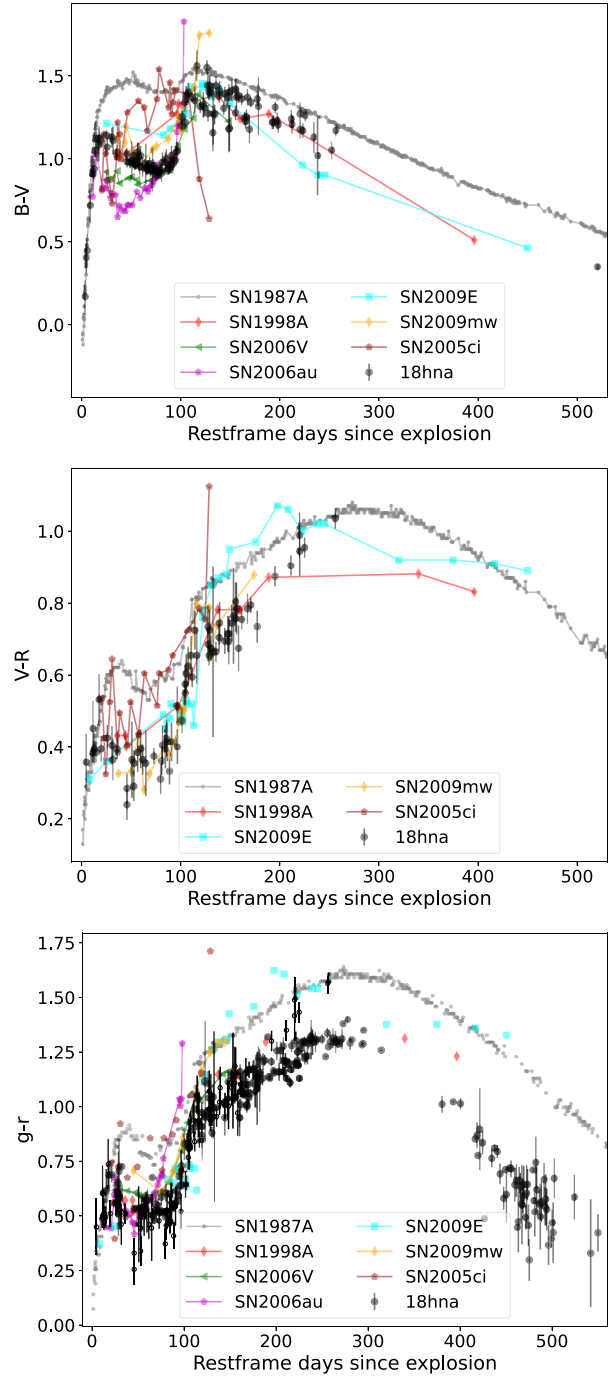


Figure 5. Colour curves of SN 2018hna compared with those of other 87A-like SNe.

around day 120. This is likely due to the growing asymmetry in the SN seen from the polarimetry Maund et al. (2021). On the other hand, it can also be a result of faster receding of the photosphere due to less mixing or clumping in the ejecta (e.g. Dessart et al. 2018). The weak absorption component in $H\alpha$ and the vanishing of $H\beta$ between days 19 and 36 can also be a result of interaction (e.g. Dessart & Hillier 2022). After day 119, when the photosphere has receded to the inner H-poor region, the emission lines of Ca II and [Ca II] in the models grow faster, implying less calcium in the inner ejecta.

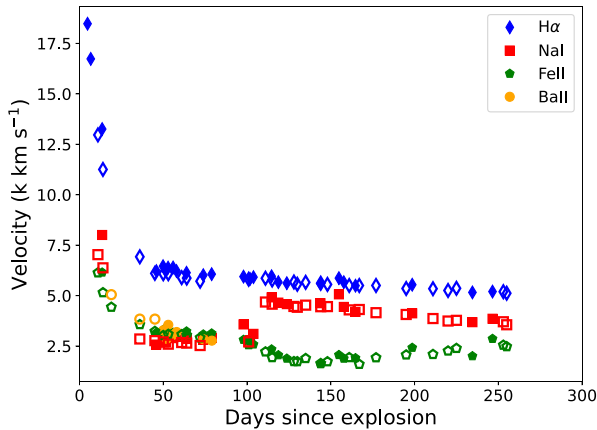


Figure 6. Expansion velocities of SN 2018hna inferred from $H\alpha$, Na I D, Fe II $\lambda 5169$, and Ba II $\lambda 6142$ absorption in the spectra. Open data points represent measurements from data available in the literature (Singh et al. 2019).

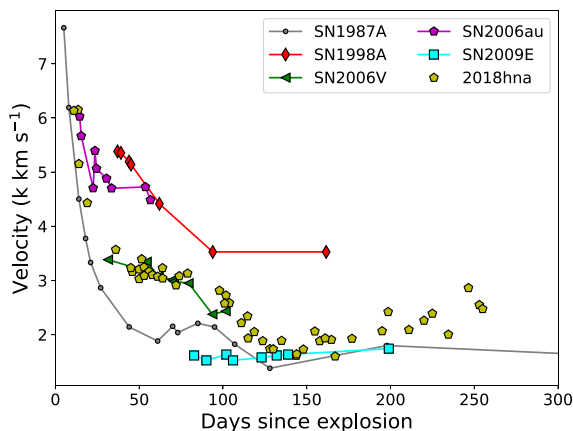


Figure 7. Fe II line velocities of SN 2018hna in comparison with several other 87A-like SNe.

4.3 Ba II line strength in 87A-like SNe

The characteristic features of Ba II absorption lines in 87A-like SNe are evident in the spectra (> 15 d) of SN 2018hna (Singh et al. 2019). A previous study by Takáts et al. (2016) found that the strength (pseudo-equivalent widths; pEWs) of the Ba II line in 87A-like SNe appears to split into two groups: the stronger group like SN 1987A and SN 2009E and the weaker one with Ba II lines similar to some normal SNe IIP (Pastorello et al. 2005). Spectra of SN 2018hna start to show significant absorption features of Ba II and Sc II since +20 d (see also Singh et al. 2019). We measured the pEWs of its Ba II $\lambda 6142$ line and compared them with those of other 87A-like SNe. As shown in the upper panel of Fig. 10, SN 2018hna can be put into the group of weaker Ba II $\lambda 6142$ absorption like SN 1998A and SN 2009mw.

In principle, the strength of Ba II lines can be affected by the following factors: an intrinsic difference in Ba abundance of the H-rich ejecta, different physical conditions such as temperature (Mazzali & Chugai 1995) and clumping in SN ejecta (Dessart et al. 2018). Among these factors, temperature may play an important role in the strength of Ba II lines, as the optical depth of Ba II lines increases with decreasing temperature. Thus, a lower mass of ^{56}Ni might be responsible for stronger Ba II lines, especially after the recombination phase when the SN is mainly powered by ^{56}Ni decay.

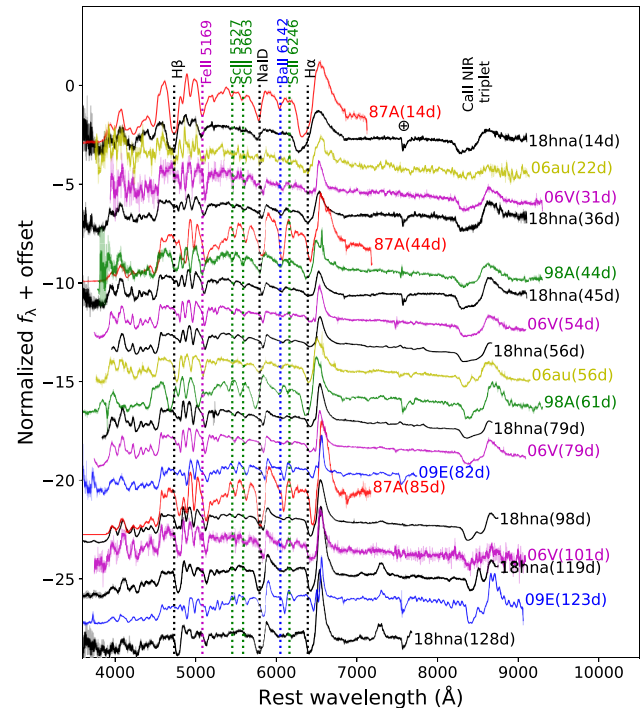


Figure 8. Spectra of SN 2018hna compared with those of other 87A-like SNe at photospheric phases. All spectra are corrected for extinction using the Milky Way law (Fitzpatrick 1999). Numbers in brackets are the corresponding phases after explosion. All spectra are normalized by dividing by their average fluxes, and also shifted vertically for clarity.

To further examine quantitatively the temperature effect on Ba II absorption, we show the pEWs of Ba II $\lambda 6142$ and the $B - V$ colour in lower panel of Fig. 10. As it can be seen, these two observables show a strong positive correlation, although there is a large variation at the red side. This suggests that low temperature be at least one of the main factors responsible for strong Ba II lines in 87A-like SNe. Note that the temperature of SNe II is related to their explosion energy and initial radius before recombination ends, and later radioactive decay is heating the ejecta. Thus, we may expect that SNe with lower specific energy (E/M) can have stronger Ba II lines in their photospheric phases, and those with lower ^{56}Ni mass can have stronger Ba II lines in the late nebular phases.

Nevertheless, differences in temperature cannot fully explain the Ba problem. For example, at $t \sim 100$ d when all 87A-like SNe share similar $B - V$ color (and hence temperature), their Ba II lines still show large scatter in strength. Thus, Ba may be abundant in some 87A-like SNe. Known mechanisms of blue–red–blue evolution of the progenitors of 87A-like SNe are related to He mixing, and therefore to the synthesis of Ba. He mixed into the outer envelope of the progenitor star can be a result of unique convection in the envelope or processes involving binary systems or stellar mergers. So the possible Ba enhanced events (e.g. SN 1987A and SN 2009E) might have more He mixed into the outer H-rich envelope.

5 BOLOMETRIC LIGHT CURVE AND HYDRODYNAMIC MODELLING

The bolometric light curve of SN 2018hna is established via the following two methods: (1) calculating the UV-through-IR (UVOIR) bolometric luminosity by integrating fluxes from optical through NIR wavebands, with the NIR light curves taken from Singh et al.

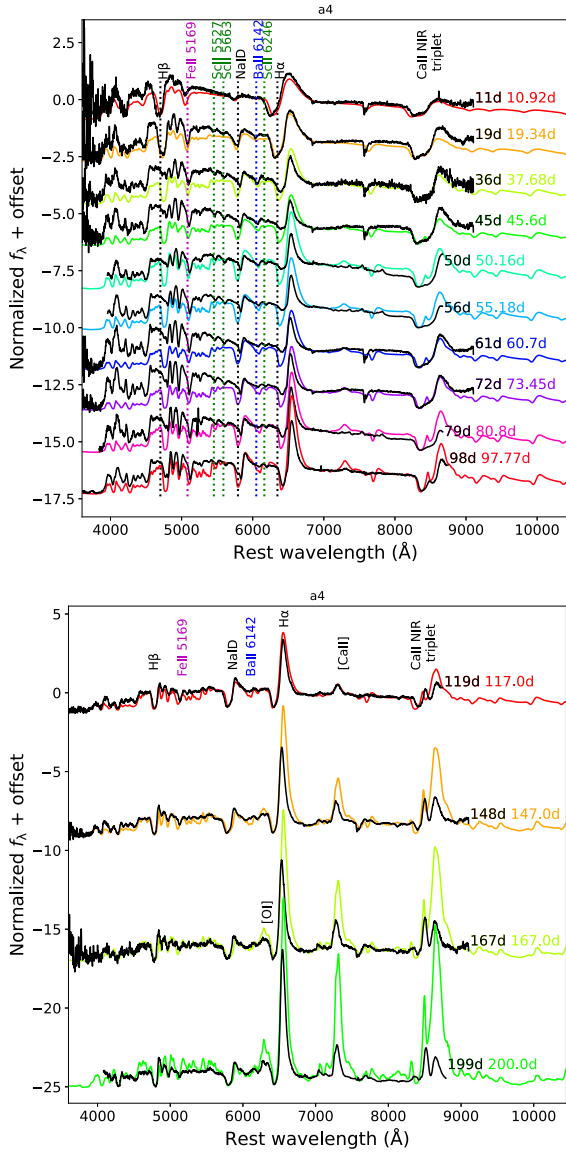


Figure 9. Comparison of the spectra of SN 2018hna in the nebular phases (<100 d; upper) and early nebular phases (100–200 d; lower) with model a4. Model spectra are plotted with coloured lines, and the phase of each spectrum is indicated by the text of the corresponding colour. Each model spectrum is normalized to match the flux within 6780–7000 Å of the overplotted observed spectrum.

(2019), noted as L_{UVOIR} ; (2) applying the bolometric correction from Lyman, Bersier & James (2014) to the $g - r$ colour of the SN, noted as L_{BC_g} . The results are shown in Fig. 11. The two methods agree well at <150 d after the explosion. We get a combined bolometric light curve of SN 2018hna using L_{UVOIR} and L_{BC_g} at $t < 150$ d. Applying an uncertainty in distance of 25 per cent, we get a peak bolometric luminosity of $L_{\text{peak}} = (6.2 \pm 3.1) \times 10^{41} \text{ erg s}^{-1}$. The bolometric light curve peaks at $\text{MJD} = 58497.4 \pm 3.5$, which gives a rise time of $t_{\text{rise}} \approx 86$ d.

5.1 Estimation of explosion parameters

Before performing light curve fitting, we first estimate the explosion parameters of SN 2018hna by quick analytical methods. The linear tail (at $t > 150$ d after explosion) of the bolometric light curve of

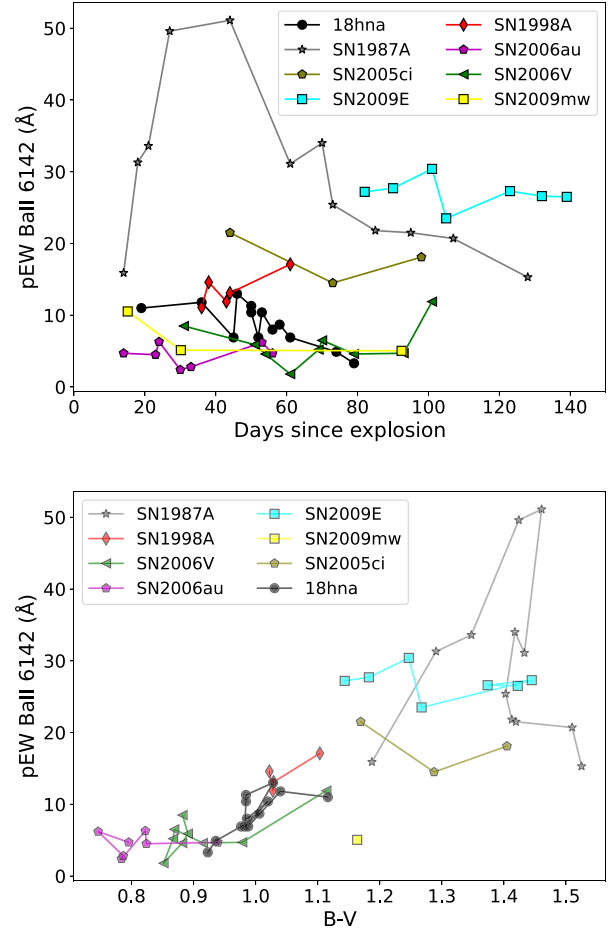


Figure 10. Upper: Pseudo-equivalent width (pEW) of the Ba II $\lambda 6142$ line of SN 2018hna compared with other 87A-like SNe. The data for SN 2009mw are taken directly from literature (Takáts et al. 2016), and data for other SNe are measured from spectra in literature. Lower: Correlation of the pEWs of Ba II $\lambda 6142$ and $B - V$ colour of 87A-like SNe.

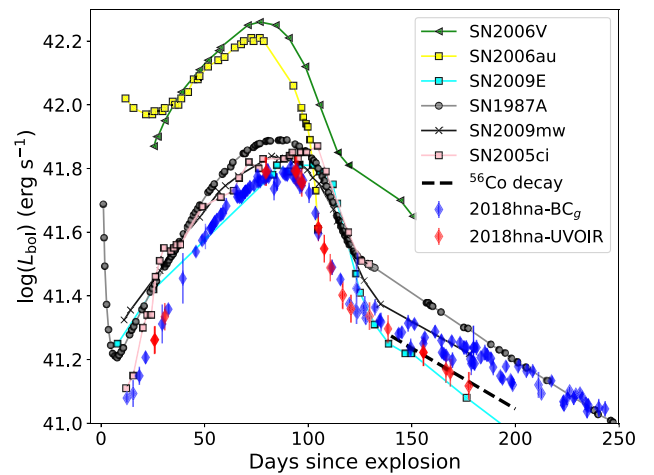


Figure 11. Bolometric light curve of SN 2018hna compared with that of other 87A-like SNe II. The red diamonds represent the bolometric light curve of SN 2018hna established with the UVOIR light curves, while the blue diamonds indicate the one derived from the ZTF gr -band light curves with bolometric corrections (see text for details). The black dashed line shows a ^{56}Ni -powered light curve with $M_{\text{Ni}} = 0.05 M_{\odot}$.

SNe II is powered by radioactive decay of ^{56}Co , and ^{56}Co is produced through the decay of ^{56}Ni . Assuming a complete γ -ray trapping, the luminosity of radioactive decay can be calculated from

$$L_{\text{Co}} = M(^{56}\text{Ni}) \epsilon_{\text{Co}} e^{-t/\tau_{\text{Co}}}. \quad (1)$$

By fitting this formula to our combined bolometric light curve at $t > 150$ d, we get an ejected ^{56}Ni mass of $\sim 0.048(\pm 0.024) M_{\odot}$. Referring to Rabinak & Waxman (2011), we estimate the radius of the progenitor by fitting the temperature evolution derived from the early spectral energy distribution (SED) of SN 2018hna. Applying $\kappa = 0.34 \text{ cm}^2 \text{ g}^{-1}$ (corresponding to fully ionized H) and $n = 3$, the best-fit parameters are $E_k = 0.9 \times 10^{51} \text{ erg}$, $R_{\star} = 45 R_{\odot}$, and $M_{\text{env}} = 11.7 M_{\odot}$. Only R_{\star} can be well constrained because the mass and kinetic energy have minor effects on temperature evolution. On the other hand, the diffusion time of radioactively-powered SNe is given as $t_d = (\kappa M_{\text{ej}} / \beta c v_{\text{ph}})^{1/2}$ (Arnett 1982; Arnett & Fu 1989), where β is a constant, v_{ph} is the photospheric velocity inferred from Fe II line near the bolometric maximum, and t_d is the rise time to peak luminosity in days. Assuming that κ is the same for SN 1987A and SN 2018hna, then we can use the parameters of SN 1987A to derive those for SN 2018hna:

$$M_{\text{ej,SN}} = M_{\text{ej,87A}} \left(\frac{t_{d,\text{SN}}}{t_{d,87A}} \right)^2 \frac{v_{\text{ph,SN}}}{v_{\text{ph,87A}}}. \quad (2)$$

Using $t_{d,87A} = 84 \text{ d}$, $v_{\text{ph,87A}} = 2200 \text{ km s}^{-1}$, $E_{87A} = 1.1 \times 10^{51} \text{ erg}$, and $M_{\text{ej,87A}} = 14 M_{\odot}$ (Blinnikov et al. 2000) for SN 1987A, we get $M_{\text{ej}} \approx 20 M_{\odot}$ and $E_k \propto M_{\text{ej}} v_{\text{ph}}^2 \approx 2.9 \times 10^{51} \text{ erg}$ for SN 2018hna by inserting its corresponding values of v_{ph} (i.e. 3000 km s^{-1}) and t_d (i.e. 86 d). Nevertheless, these estimates are very rough, and we need more detailed model fitting to get more accurate values. In the following subsection, we will use two methods to fit the bolometric light curve of SN 2018hna.

5.2 Light-curve fitting

The progenitors of 87A-like SNe are thought to be BSGs with small radius ($R < 100 R_{\odot}$) and high effective temperature ($T_{\text{eff}} > 10,000 \text{ K}$). Large density and small radius can result in a slowly-rising SN light curve. The progenitors of 87A-like SNe are thought to have evolved from different channels than those of normal SNe II. For SN 2018hna, Singh et al. (2019) modelled the early multiband light curves based on the progenitor model proposed by Blinnikov et al. (2000), yielding $E_{\text{SN}} \approx 1.7 \times 10^{51} \text{ erg}$ ($E_k \approx 0.97 \times 10^{51} \text{ erg}$) and $M_{\text{ej}} \approx 14 M_{\odot}$. However, the phase range of their fitting is limited only to the shock-cooling phase (i.e. $t < 30 \text{ d}$), and the later light curves cannot match the observations (private communication with Petr V. Baklanov). Thus, we revisit this SN by fitting the bolometric light curve to both a semi-analytical model and hydrodynamical models.

A semi-analytical light-curve model for SNe II was published by Nagy et al. (2014) and further developed in Nagy & Vinkó (2016). In this model, the SN ejecta are divided into two parts: the inner core and outer shell. As the outer shell component only contributes to the early-time shock-cooling phase, we only consider the core component. Free parameters include M_{ej} , R_0 , $M(^{56}\text{Ni})$, E_k , and the initial thermal energy $E_{\text{th},0}$. We adopt $\kappa = 0.19 \text{ cm}^2 \text{ g}^{-1}$, the average opacity of a one-dimensional (1D) model for SNe II, and the gamma-ray leakage exponent $A_g = 2.7 \times 10^5$, as Nagy & Vinkó (2016) used for SN 1987A. We modified the code by Nagy & Vinkó (2016) so that it can be used as subroutines in `python` and then applied the Markov chain Monte Carlo (MCMC) package `emcee` (Foreman-Mackey et al. 2013) to do MCMC fitting to the derived bolometric

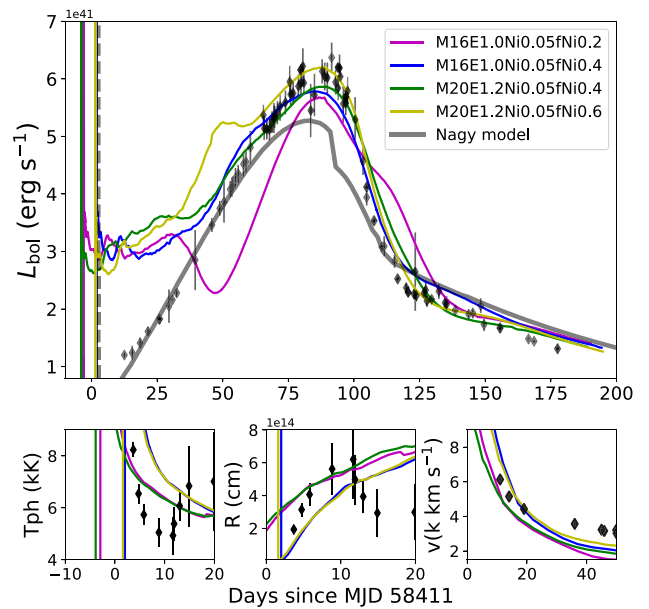


Figure 12. Bolometric light-curve models for SN 2018hna overplotted with the observed bolometric light curve (top). Light curves of models are shifted horizontally to match the peak date of the observation. The date of discovery (MJD 58413.815) is marked by the dashed vertical line. The photometric temperature, radius, and expansion velocity from STELLA models are compared to the observations (bottom). See the text for details.

light curve of SN 2018hna in the range 20–200 d after MJD = 58411. The resulting best-fit parameters are $M_{\text{ej}} = 13.29^{+0.37}_{-1.82} M_{\odot}$, $R_0 = 55^{+2}_{-9} R_{\odot}$, $M(^{56}\text{Ni}) = 0.052^{+0.001}_{-0.002} M_{\odot}$, $E_k = 3.08^{+0.15}_{-0.85} \times 10^{51} \text{ erg}$, and $E_{\text{th},0} = 0.16^{+0.02}_{-0.08} \times 10^{51} \text{ erg}$. The model light curve as well as the observed bolometric light curve of SN 2018hna are shown in Fig. 12.

We also compare with the hydrodynamical results. First, we use Modules for Experiments in Stellar Astrophysics (MESA; Paxton et al. 2011, 2013, 2015, 2018) to evolve a massive single star to core-collapse explosion. Then a quantity of energy is deposited into the innermost layer and the shock spread close to the stellar surface. Finally, the 1D radiation hydrodynamics code STELLA (Blinnikov et al. 1998, 2000, 2006) is used to compute the SN evolution.

We tested stars with an initial mass of 12–25 M_{\odot} and metallicity $Z = 10^{-6}$ – 10^{-3} using MESA. To obtain a BSG progenitor, we find that very low metallicity is needed. A star with $M = 12 M_{\odot}$ and $Z = 10^{-6}$ ends up as an RSG, and the one with $M = 16 M_{\odot}$ and $Z = 5 \times 10^{-5}$ produces a hot star with $R > 100 R_{\odot}$. The most massive model with $M = 25 M_{\odot}$ requires a metallicity lower than 10^{-3} to make a BSG SN progenitor. All models that collapse as a BSG stop evolving before they become an RSG, similar to that found by Taddia et al. (2016). We obtained two pre-SN models, one with $M_{\text{ZAMS}} = 16 M_{\odot}$ and $Z = 10^{-6}$, the other with $M_{\text{ZAMS}} = 20 M_{\odot}$ and $Z = 10^{-6}$. These two models are exploded in MESA with a final energy of 1.0×10^{51} and $1.2 \times 10^{51} \text{ erg}$, respectively. The $16 M_{\odot}$ model has a remnant mass of $2.3 M_{\odot}$ ($M_{\text{ej}} = 13.7 M_{\odot}$) and $R = 44 R_{\odot}$; the $20 M_{\odot}$ model has a remnant mass of $2.32 M_{\odot}$ ($M_{\text{ej}} = 17.7 M_{\odot}$) and $R = 50 R_{\odot}$. The final masses are almost the same as the initial masses owing to the low metallicity. We use these two models to explore the mass range of the SN ejecta.

To match the bolometric light curve of SN 2018hna, we vary the following parameters: total energy of SN explosion, ^{56}Ni mass in the ejecta, and mixing length of the ^{56}Ni distribution; ^{56}Ni is uniformly distributed from the innermost shell to a fraction f_{Ni} of the total mass.

We find that the slow rise and steep decline around the main peak can be explained by a moderate mixing of ^{56}Ni ($f_{\text{Ni}} = 0.4$). With more ^{56}Ni mixed into the outer ejecta, an additional peak would emerge before the main peak. The 16 and 20 M_{\odot} models can both fit the bolometric light curve except for the shock-cooling phase. This is a result of high temperature of the MESA model, leading to high shock-cooling luminosity. The 16 M_{\odot} model requires a first-light date quite close to the discovery, while the first-light date of the 20 M_{\odot} model is about 4 d prior to that found by Singh et al. (2019) with early shock cooling light curve fitting. We would expect that any models with $M_{\text{ej}} \lesssim 13.7 M_{\odot}$ would have rise times shorter than 83.6 d, which is the time from discovery to maximum light, thus unlikely for SN 2018hna. If we consider the estimate of explosion epoch by Singh et al. (2019) to be relatively accurate, then the ejecta mass of the SN tends to be less than 17.7 M_{\odot} .

The main difference between the explosion parameters yielded by the semi-analytical model and the hydrodynamical models is that the former produces a kinetic energy about twice the latter. The hydrodynamical models may be more plausible, as the ratio of kinetic energy to ^{56}Ni mass found by the semi-analytical model seems too high for a core-collapse supernova. According to our STELLA models, SN 2018hna has ejecta mass larger than $\sim 13.7 M_{\odot}$ but less than $\sim 17.7 M_{\odot}$. Assuming a remnant mass of 1.4 M_{\odot} , the pre-explosion star should be more massive than 15 M_{\odot} . We further discuss the possible origin of the progenitor of SN 2018hna in Section 6.

6 DISCUSSIONS

In this section, we further discuss the progenitor properties of SN 2018hna and the 87A-like SNe II by comparing the [O I] line features and the deduced oxygen mass in the SN ejecta with those predicted by stellar evolution models.

6.1 [O I] line properties

In Section 5, we derived some explosion parameters for SN 2018hna, helping constrain its progenitor properties. Here, we examine the

progenitor properties using nebular-phase spectra, especially the [O I] lines.

The strength of the [O I] $\lambda 5577$ and [O I] $\lambda\lambda 6300, 6364$ lines in nebular spectra of core-collapse SNe can be used to roughly estimate the ejected oxygen mass in the SN explosion (Uomoto & Kirshner 1986; Li & McCray 1992; Chugai 1994; Jerkstrand et al. 2014). Using the nebular spectra, we measure the flux of the [O I] $\lambda 5577$ and [O I] $\lambda\lambda 6300, 6364$ lines of SN 2018hna. For comparison, we collected nebular spectra for other 87A-type SNe and performed similar analysis for them. Besides SN 1987A, the nebular spectra are only available for SN 1998A and SN 2009E. The mass of oxygen is calculated using the eqs. 2 and 3 from Jerkstrand et al. (2014). We summarize the observations, measurement results of oxygen lines and the inferred mass of oxygen in Table 1.

The oxygen mass of SN 2018hna is found to be 0.43–0.73 M_{\odot} close to that of SN 1998A (0.52 M_{\odot}), but significantly lower than that of SN 1987A (1.10–1.65 M_{\odot}). The result derived for SN 1987A is consistent with that inferred in the literature (1.2–1.5 M_{\odot} ; Li & McCray 1992; Chugai 1994; Kozma & Fransson 1998), but our results for SN 1998A (0.52 M_{\odot}) and SN 2009E (0.13–0.46 M_{\odot}) are lower than those estimated by Pastorello et al. (2012a) (i.e. 1.18–1.48 M_{\odot} for SN 1998A and 0.60–0.75 M_{\odot} for SN 2009E). Differences in the derived oxygen mass are likely related to the methods adopted in the calculations. For example, when adopting equation 3 of Pastorello et al. (2012a), the oxygen mass of SN 2009E is estimated as 0.5–0.6 M_{\odot} which is slightly larger than our result; while the corresponding estimates are 0.51–0.63 M_{\odot} for SN 1998A and 0.43–0.65 M_{\odot} for SN 2018hna, respectively, which are similar to our results.

Standard stellar evolution theories predict that the oxygen mass in the SN ejecta is positively correlated with the initial mass of the exploding star (e.g. Woosley & Weaver 1995). Metallicity of the host galaxy of SN 2018hna is found to be about 0.3 Z_{\odot} (Singh et al. 2019). While considering that the SN is located far from the galaxy centre, SN 2018hna could be metal-poorer (i.e. $Z < 0.3 Z_{\odot}$). Comparing the ejected oxygen mass derived for SN 2018hna with that predicted by standard single star evolution models at different metallicities ($Z = Z_{\odot}$, Sukhbold et al. (2016) and $Z = 0.1 Z_{\odot}$, Woosley & Weaver

Table 1. Nebular spectral properties of 87A-like supernovae.

SN	M_{Ni} (M_{\odot})	Phase (d)	$L([\text{O I}] \lambda\lambda 6300, 6364)$ (erg s^{-1})	$L([\text{O I}] \lambda 5577)$ (erg s^{-1})	$M([\text{O I}]_{\beta_{\text{ratio}}=1.5, \beta_{6300}=0.5}^{\text{LTE}})$ (M_{\odot})	Data source
SN 1987A	0.075	198	3.62×10^{39}	5.74×10^{38}	1.33	1
		339	2.36×10^{39}	1.81×10^{38}	1.65	1
		360	2.01×10^{39}	1.44×10^{38}	1.49	1
		375	1.85×10^{39}	1.21×10^{38}	1.48	1
		408	1.40×10^{39}	8.38×10^{37}	1.22	1
		428	1.21×10^{39}	6.84×10^{37}	1.10	1
		526	3.44×10^{38}	1.64×10^{37}	0.37	1
		SN 1998A	0.11	161	2.34×10^{39}	6.57×10^{38}
343	1.45×10^{39}	Not covered		–	2	
416	2.82×10^{38}	–		–	2	
SN 2009E	0.04	198	6.44×10^{38}	2.13×10^{38}	0.13	3
		226	6.73×10^{38}	1.54×10^{38}	0.19	3
		386	3.69×10^{38}	1.56×10^{37}	0.46	3
		388	3.07×10^{38}	$< 3.29 \times 10^{37}$	> 0.17	3
SN 2018hna	0.05	247	1.59×10^{39}	2.10×10^{38}	0.73	This work
		253	1.13×10^{39}	1.77×10^{38}	0.44	4
		255	1.16×10^{39}	1.56×10^{38}	0.53	4
		522	9.61×10^{37}	–	–	This work

Note. **References.** (1) Pun et al. (1995); (2) Pastorello et al. (2005); (3) Pastorello et al. (2012b); (4) Singh et al. (2019).

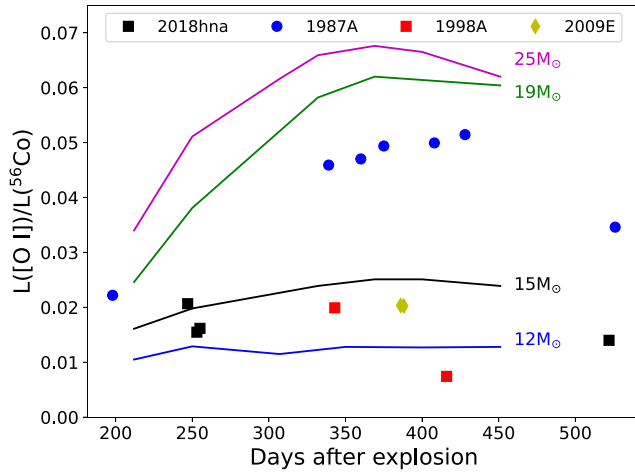


Figure 13. The nebular-phase evolution of [O I] $\lambda\lambda$ 6300, 6364 line luminosities (normalized to the ^{56}Co decay power) of four 87A-like SNe, compared with model predictions. The solid lines represent the model predictions with initial masses of $12 M_{\odot}$ (blue), $15 M_{\odot}$ (black), $19 M_{\odot}$ (green), and $25 M_{\odot}$ (pink), respectively.

(1995)), the initial mass of SN 2018hna is constrained to have a range of $12\text{--}15.5 M_{\odot}$, while a corresponding range of $16\text{--}19 M_{\odot}$ is found for SN 1987A. The low initial masses of SNe 2018hna, 1998A and 2009E are in agreement with low mass NLTE spectra models (see Appendix A for details). The distinction between SN 1987A and the other three 87A-like SNe can also be seen from the evolution of their [O I] line luminosities. Like in Jerkstrand et al. (2015), we compare the evolution of nebular [O I] $\lambda\lambda$ 6300, 6364 luminosity with that of the models from Jerkstrand et al. (2014) in Fig. 13. Among the four 87A-like objects, only SN 1987A lies above the $15 M_{\odot}$ model, while the other three show the distribution similar to normal SNe II (see fig. 9 of Jerkstrand et al. 2015).

Through the above analysis of the nebular [O I] lines, we find that under the assumption of standard single-star evolution, the initial mass of the progenitor star of SN 2018hna will not exceed $16 M_{\odot}$. However, in standard single-star evolution model, a star with $M_{\text{ZAMS}} \lesssim 16 M_{\odot}$ will evolve to be a BSG prior to core collapse only under extremely low metallicity ($Z \approx 10^{-6}$) condition. This is not the case of any 87A-like SNe, which implies that the progenitor stars of 87A-like SNe are unlikely to have evolved as a single star through standard evolution. Instead, some non-standard mechanisms are needed, or the progenitor stars are involved in binary or multiple systems. As for SN 1987A, a binary scenario is more favourable. We notice that the large gap of [O I] line properties between SN 1987A and others may indicate that their progenitors are essentially different, although similar ejected mass and energy can be derived from their light curves. In the next subsection, we will extend our discussions about the possible progenitor origins of SN 2018hna.

6.2 Possible origins of the progenitors of 87A-like SNe

It is now well known that 87A-like SNe are located in lower metallicity galaxies than SNe IIP, and the partially stripped type IIB SNe have a similar metallicity distribution to that of 87A-like SNe (e.g. Taddia et al. 2013). Apparently, differences in metallicity alone cannot make stars evolve in such different ways, since most H-rich SNe arising from similar metal-poor environment tend to become Type IIP (e.g. SN 2015bs arising from $Z \lesssim 0.1 Z_{\odot}$; Anderson et al. 2018). According to standard stellar evolution theory, stars

with initial masses in a range of 8 to $30 M_{\odot}$ would end up as RSGs, although no RSG progenitor with mass $>20 M_{\odot}$ has been found yet. Archival images of SNe IIP progenitors indicate an average initial mass of $\sim 10 M_{\odot}$ (Smartt 2015). Progenitors of 87A-like SNe are not settled yet, while there are several possibilities for both single stars and binaries. We discuss these probabilities below.

The ejecta mass of 87A-like SNe can be derived from their light curves using empirical relations – the relation between diffusion time, SN energy, and mass (Arnett & Fu 1989) – or analytical/hydrodynamical light-curve models (e.g. Arnett 1980; Blinnikov et al. 2000; Zampieri et al. 2003; Nagy et al. 2014; Nagy & Vinkó 2016). By examining these SNe, we find that their ejecta masses lie in the range of $\sim 12\text{--}26 M_{\odot}$, with a typical value of $\sim 17 M_{\odot}$. It seems that 87A-like SNe have higher ejected total mass as well as ^{56}Ni mass than normal SNe IIP, while they share similar velocity evolution (see Fig. 7). Thus, we conclude that 87A-like SNe have more massive progenitors and suffer more energetic explosions than normal SNe II. However, it is shown above that some 87A-like SNe should be relatively oxygen-poor, with SN 1987A itself being an exception. Progenitors of those oxygen-poor 87A-like events are likely to be generated through different channels than SN 1987A.

There must be some mechanisms that reduce the oxygen mass in SN ejecta. It is believed that the progenitor star of SN 1987A has undergone blue–red–blue evolution; the abundance ratios of N/C and N/O in the circumstellar gas around the SN are large compared to solar ratios, which was interpreted as an evidence of experiencing mass-loss when the star was an RSG. The conditions under which this process occurs were investigated by Saio, Kato & Nomoto (1988), and they concluded that either high envelope mass or enhanced He abundance (Y) in the H-rich envelope after core He burning is needed. High envelope mass can be a result of unusually low metallicity and zero mass-loss (e.g. Weiss, Hillebrandt & Truran 1988, but it was ruled out for SN 1987A) or simply higher initial mass. Apparently, the low oxygen mass derived above indicates that SN 2018hna (also SN 1998A and SN 2009E) cannot be produced by a single massive star with standard evolution; we need other mechanisms. Higher Y can be acquired by mixing due to semiconvection and shell convection or rotation. It is easier to reach the acquired Y under lower metallicity.

Single-star models for a BSG SN progenitor have been discussed extensively in literature (Arnett 1987; Hillebrandt et al. 1987; Saio et al. 1988; Weiss et al. 1988; Woosley et al. 1988; Weiss 1989; Langer 1991; Petermann et al. 2015; Utrobin et al. 2019). Utrobin et al. (2019) calculated the explosion of several single-star models; their B15-2, W16-3, W18x2, and W20 all have ejected oxygen mass $<0.7 M_{\odot}$, with B15 having the least amount of oxygen (i.e. $0.16 M_{\odot}$). Considering both ejecta mass and oxygen mass, W16-3 is suitable for SN 2018hna. The progenitor of the W16-3 model is evolved by invoking reduced metallicity ($Z = 1/3 Z_{\odot}$, close to that of SN 2018hna), restricted semiconvection, and a substantial amount of rotation ($J_{\text{ZAMS}} = 2.7 \times 10^{52}$ erg; Sukhbold et al. 2016). So, it is still likely that these oxygen-poor events originated from a single-star channel.

If the progenitor star has been in a binary system, accretion from the companion or merging of the stars can enlarge the envelope hence produce BSG SN progenitors. Binary models have been presented by Podsiadlowski & Joss (1989), Hillebrandt & Meyer (1989), Podsiadlowski, Joss & Hsu (1992) with binary interaction (mass transfer), Podsiadlowski, Morris & Ivanova (2007), Menon & Heger (2017), and Utrobin et al. (2021) with star mergers. These models successfully match the properties of SN 1987A and its progenitor star, especially the triple-ring nebula around it, which is a direct

evidence of a star merger. It is also possible that the progenitors of the oxygen-poor events were evolved from binary interaction, but the ejected oxygen masses are substantially smaller than that of SN 1987A, hence much lower initial mass of the binary system. This may also be related to the lower ratio of oxygen-rich events (so far only 1 out of 4), as the proportion of lower-mass stars is thought to be higher. In addition, the rarity of 87A-like events in SNe II is also in line with the expectations of binary star evolution (Podsiadlowski et al. 1992; Woosley, Heger & Weaver 2002). In the case of SN 2018hna, the similar polarization properties to SN 1987A might also make the binary picture more favourable.

7 SUMMARY

The peculiar H-rich SN 2018hna is studied with new optical photometry and spectra presented in addition to those by Singh et al. (2019). Like SN 1987A, SN 2018hna shows a slow rise to maximum light in ~ 86 d, with a peak bolometric luminosity of $(6.2 \pm 3.1) \times 10^{41}$ erg s $^{-1}$. A ^{56}Ni mass of $(0.048 \pm 0.024) M_{\odot}$ was derived from the linear declining tail after 150 d. Both the photometric and spectroscopic evolution of SN 2018hna behave like the famous SN 1987A, making it another well-observed peculiar SN II with observations covering from the early shock-cooling phase to more than 550 d after the explosion.

In addition, we collected a small sample of 87A-like SNe II with good photometric and spectroscopic observations in the literature and studied some of their properties in comparison with SN 2018hna. The $B - V$ colour curves of 87A-like SNe all show two peaks, and they share similar evolution before the first peak and after the second peak ($t > 100$ d). For them, we find that the earlier the first peak occurs, the shorter time it will take the $B - V$ colour to go redward again. The expansion velocity evolution of SN 2018hna is among the range of the 87A-like SN family. In the photospheric phase, the spectral evolution of SN 2018hna shows high resemblances to SN 2006V, with weak metal lines and H α absorption. Metal lines, such as Fe II and Ba II are unusually strong among this subtype. We measured the pEW of the Ba II $\lambda 6142$ line in the spectra of 87A-like SNe; and we found that it is significantly stronger in SN 1987A and SN 2009E than in other objects. The pEW of Ba II $\lambda 6142$ is positively related to the $B - V$ colour of the SNe, implying that low temperature may be the leading factor responsible for strong Ba II lines. Nevertheless, the photospheric temperature cannot fully explain the observed difference. Some Ba-strong events are found to have real enhanced Ba abundance in their ejecta. In addition, lower ^{56}Ni mass might also be responsible for stronger Ba II lines. Further studies are needed for definite conclusions.

We calculated the bolometric light curve of SN 2018hna using its multiband light curves; a stellar radius of $R \approx 45 R_{\odot}$ is derived from the temperature evolution. Two methods were used to fit the bolometric light curve of SN 2018hna to estimate its explosion parameters. Using the semi-analytical model by Nagy & Vinkó (2016), we found a best-fit model with $M_{\text{ej}} \approx 13.29 M_{\odot}$, $R_0 \approx 55 R_{\odot}$, $M(^{56}\text{Ni}) \approx 0.052 M_{\odot}$, $E_k \approx 3.08 \times 10^{51}$ erg, and $E_{\text{th},0} = 0.16 \times 10^{51}$ erg. The ratio of E_k to $M(^{56}\text{Ni})$ given by this model seems too high for a core-collapse supernova. On the other hand, the hydrodynamic method (built by MESA and STELLA) gives more plausible fit with $M_{\text{ej}} = 13.7\text{--}17.7 M_{\odot}$, $E_k = 1.0\text{--}1.2 \times 10^{51}$ erg, $M_{^{56}\text{Ni}} = 0.05 M_{\odot}$, and ^{56}Ni mixing length scale $f_{\text{Ni}} = 0.4$.

In order to study the properties of the progenitor star of SN 2018hna, we investigated the luminosities of the [O I] lines in

its nebular phase spectra. As comparison, we also collected nebular spectra of other 87A-like SNe and found two of them (SN 1998A and SN 2009E) in addition to SN 1987A. The nebular [O I] lines are used to estimate the ejected oxygen masses, and hence the initial masses of their progenitors. We estimated the ejected oxygen mass of SN 2018hna to be $0.44\text{--}0.73 M_{\odot}$ using the [O I] $\lambda 5577$ and [O I] $\lambda\lambda 6300, 6364$ lines in the nebular spectra. Similar low oxygen masses were found for SN 1998A and SN 2009E. SN 1987A has significantly larger mass of ejected oxygen ($1.10\text{--}1.65 M_{\odot}$). The distinction between SN 1987A and SN 2018hna can also be seen from their evolution of the luminosities of nebular [O I] $\lambda\lambda 6300, 6364$ lines.

The gap in ejected oxygen mass and behaviour of [O I] lines in the nebular spectra seen between SN 1987A and SN 2018hna indicate that their progenitors were probably formed through different channels. Some single-star models with reduced metallicity, restricted semiconvection, and a substantial amount of rotation from Sukhbold et al. (2016) might match the low oxygen mass of SN 2018hna. Unlike in the case of SN 1987A where the single-star picture is almost ruled out, it is possible that SN 2018hna was originated from a single massive star. On the other hand, the binary scenario can be plausible. Given the dominance of binary interactions in the evolution of massive stars, and the similar polarization properties to SN 1987A, the binary scenario may be more likely for SN 2018hna. In the binary picture, the low oxygen mass in SN 2018hna may be a result of lower masses of the binary components or less material that was accreted from the companion. More observational and theoretical research is required to uncover the mystery of BSG supernova progenitors. The oxygen mass in SN ejecta can be a key point in future studies, and analysis of the explosion rate of 87A-like SNe can be helpful.

ACKNOWLEDGEMENTS

We acknowledge the support of the staff of the XLT, LJT, TNT, ARC, and Keck-I for assistance with the observations. The operation of XLT is supported by the Open Project Program of the Key Laboratory of Optical Astronomy, National Astronomical Observatories, Chinese Academy of Sciences. Funding for the LJT has been provided by the Chinese Academy of Sciences and the People's Government of Yunnan Province. The LJT is jointly operated and administrated by Yunnan Observatories and Center for Astronomical Mega-Science, CAS. Some of the data presented herein were obtained at the W. M. Keck Observatory, which is operated as a scientific partnership among the California Institute of Technology, the University of California, and NASA; the observatory was made possible by the generous financial support of the W. M. Keck Foundation. Distance and Galactic extinction to SN 2018hna are obtained via the NASA/IPAC Extragalactic Database (NED). Photometric and spectral data of referenced SNe were obtained via the the Open Supernova Catalog (OSC; Guillochon et al. 2017) and the Weizmann Interactive Supernova Data Repository (WiSeREP; Yaron & Gal-Yam 2012). The ZTF forced-photometry service was funded under Heising-Simons Foundation grant #12540303 (PI, M. Graham).

This work is supported by the National Natural Science Foundation of China (NSFC grants 12288102, 12033003, and 11633002), the Scholar Program of Beijing Academy of Science and Technology (DZ:BS202002), and the TencentXplorer Prize. A.V.F.'s group at U.C. Berkeley received financial support from the Christopher R. Redlich Fund and many individual donors. SB is supported by grant RSF 19-12-00229 for the development of STELLA code.

DATA AVAILABILITY

Photometric data of SN 2018hna from the TNT and ZTF are presented in Tables C2 and C3. Spectroscopic data are available on reasonable request to the corresponding authors.

REFERENCES

- Anderson J. P. et al., 2014, *ApJ*, 786, 67
 Anderson J. P. et al., 2018, *Nature Astronomy*, 2, 574
 Arnett W. D., 1980, *ApJ*, 237, 541
 Arnett W. D., 1982, *ApJ*, 253, 785
 Arnett W. D., 1987, *ApJ*, 319, 136
 Arnett W. D., Fu A., 1989, *ApJ*, 340, 396
 Bellm E. C. et al., 2019, *PASP*, 131, 018002
 Bevan A., 2018, *MNRAS*, 480, 4659
 Bevan A., Barlow M. J., 2016, *MNRAS*, 456, 1269
 Bevan A. M. et al., 2020, *ApJ*, 894, 111
 Blinnikov S. I., Eastman R., Bartunov O. S., Popolitov V. A., Woosley S. E., 1998, *ApJ*, 496, 454
 Blinnikov S., Lundqvist P., Bartunov O., Nomoto K., Iwamoto K., 2000, *ApJ*, 532, 1132
 Blinnikov S. I., Röpke F. K., Sorokina E. I., Gieseler M., Reinecke M., Travaglio C., Hillebrandt W., Stritzinger M., 2006, *A&A*, 453, 229
 Catchpole R. M. et al., 1987, *MNRAS*, 229, 15P
 Catchpole R. M. et al., 1988, *MNRAS*, 231, 75P
 Chugai N. N., 1994, *ApJ*, 428, L17
 Chugai N. N., 2001, *MNRAS*, 326, 1448
 Dessart L., Hillier D. J., 2005, *A&A*, 437, 667
 Dessart L., Hillier D. J., 2008, *MNRAS*, 383, 57
 Dessart L., Hillier D. J., 2010, *MNRAS*, 405, 2141
 Dessart L., Hillier D. J., 2019, *A&A*, 622, A70
 Dessart L., Hillier D. J., 2022, *A&A*, 660, L9
 Dessart L., Hillier D. J., Wilk K. D., 2018, *A&A*, 619, A30
 Dessart L., Hillier D. J., Sukhbold T., Woosley S. E., Janka H. T., 2021, *A&A*, 652, A64
 Falco E. E. et al., 1999, *PASP*, 111, 438
 Filippenko A. V., 1997, *ARA&A*, 35, 309
 Fitzpatrick E. L., 1999, *PASP*, 111, 63
 Foreman-Mackey D., Hogg D. W., Lang D., Goodman J., 2013, *PASP*, 125, 306
 Gal-Yam A., 2017, in Alsabti A. W., Murdin P., eds, *Handbook of Supernovae*. Springer, Berlin
 Gehrels N. et al., 2004, *ApJ*, 611, 1005
 Guillochon J., Parrent J., Kelley L. Z., Margutti R., 2017, *ApJ*, 835, 64
 Gutiérrez C. P. et al., 2017, *ApJ*, 850, 89
 Hamuy M., Pinto P. A., 2002, *ApJ*, 566, L63
 Hillebrandt W., Meyer F., 1989, *A&A*, 219, L3
 Hillebrandt W., Hoefflich P., Weiss A., Truran J. W., 1987, *Nature*, 327, 597
 Hoefflich P., 1988, *PASA*, 7, 434
 Huang F., Li J.-Z., Wang X.-F., Shang R.-C., Zhang T.-M., Hu J.-Y., Qiu Y.-L., Jiang X.-J., 2012, *Res. Astron. Astrophys.*, 12, 1585
 Ivezić Ž. et al., 2007, *AJ*, 134, 973
 Jerkstrand A., Smartt S. J., Fraser M., Fransson C., Sollerman J., Taddia F., Kotak R., 2014, *MNRAS*, 439, 3694
 Jerkstrand A. et al., 2015, *MNRAS*, 448, 2482
 Jordi K., Grebel E. K., Ammon K., 2006, *A&A*, 460, 339
 Karachentsev I. D., Makarov D. I., Kaisina E. I., 2013, *AJ*, 145, 101
 Kelly P. L. et al., 2016, *ApJ*, 831, 205
 Kleiser I. K. W. et al., 2011, *MNRAS*, 415, 372
 Kozma C., Fransson C., 1998, *ApJ*, 497, 431
 Langer N., 1991, *A&A*, 243, 155
 Li H., McCray R., 1992, *ApJ*, 387, 309
 Lyman J. D., Bersier D., James P. A., 2014, *MNRAS*, 437, 3848
 Maund J. R. et al., 2021, *MNRAS*, 503, 312
 Mazzali P. A., Chugai N. N., 1995, *A&A*, 303, 118
 Mazzali P. A., Lucy L. B., Butler K., 1992, *A&A*, 258, 399
 Menon A., Heger A., 2017, *MNRAS*, 469, 4649
 Menzies J. W. et al., 1987, *MNRAS*, 227, 39P
 Nagy A. P., Vinkó J., 2016, *A&A*, 589, A53
 Nagy A. P., Ordasi A., Vinkó J., Wheeler J. C., 2014, *A&A*, 571, A77
 Niculescu-Duvaz M. et al., 2022, *MNRAS*, 515, 4302
 Oke J. B. et al., 1995, *PASP*, 107, 375
 Pastorello A. et al., 2005, *MNRAS*, 360, 950
 Pastorello A. et al., 2012a, *A&A*, 537, A141
 Pastorello A. et al., 2012b, *A&A*, 537, A141
 Paxton B., Bildsten L., Dotter A., Herwig F., Lesaffre P., Timmes F., 2011, *ApJS*, 192, 3
 Paxton B. et al., 2013, *ApJS*, 208, 4
 Paxton B. et al., 2015, *ApJS*, 220, 15
 Paxton B. et al., 2018, *ApJS*, 234, 34
 Perley D. A. et al., 2020, *ApJ*, 904, 35
 Petermann I., Langer N., Castro N., Fossati L., 2015, *A&A*, 584, A54
 Podsiadlowski P., 1992, *PASP*, 104, 717
 Podsiadlowski P., Joss P. C., 1989, *Nature*, 338, 401
 Podsiadlowski P., Joss P. C., Hsu J. J. L., 1992, *ApJ*, 391, 246
 Podsiadlowski P., Morris T. S., Ivanova N., 2007, in Immler S., Weiler K., McCray R., eds, *AIP Conf. Ser. Vol. 937, Supernova 1987A: 20 Years After: Supernovae and Gamma-Ray Bursters*. Am. Inst. Phys., New York, p. 125
 Pun C. S. J. et al., 1995, *ApJS*, 99, 223
 Rabinak I., Waxman E., 2011, *ApJ*, 728, 63
 Rho J. et al., 2019, *Astron. Telegram*, 12897, 1
 Roming P. W. A. et al., 2005, *Space Sci. Rev.*, 120, 95
 Saio H., Kato M., Nomoto K., 1988, *ApJ*, 331, 388
 Schlafly E. F., Finkbeiner D. P., 2011, *ApJ*, 737, 103
 Singh A. et al., 2019, *ApJ*, 882, L15
 Smartt S. J., 2015, *PASA*, 32, e016
 Sukhbold T., Ertl T., Woosley S. E., Brown J. M., Janka H. T., 2016, *ApJ*, 821, 38
 Suntzeff N. B., Hamuy M., Martin G., Gomez A., Gonzalez R., 1988, *AJ*, 96, 1864
 Taddia F. et al., 2012, *A&A*, 537, A140
 Taddia F. et al., 2013, *A&A*, 558, A143
 Taddia F. et al., 2016, *A&A*, 588, A5
 Takáts K. et al., 2016, *MNRAS*, 460, 3447
 Tinyanont S. et al., 2021, *Nature Astronomy*, 5, 544
 Uomoto A., Kirshner R. P., 1986, *ApJ*, 308, 685
 Utrobin V. P., Wongwathanarat A., Janka H. T., Müller E., Ertl T., Woosley S. E., 2019, *A&A*, 624, A116
 Utrobin V. P., Wongwathanarat A., Janka H. T., Müller E., Ertl T., Menon A., Heger A., 2021, *ApJ*, 914, 4
 Wampler E. J., Wang L., Baade D., Banse K., D’Odorico S., Gouiffes C., Tarengi M., 1990, *ApJ*, 362, L13
 Wang X. et al., 2008, *ApJ*, 675, 626
 Weiss A., 1989, *ApJ*, 339, 365
 Weiss A., Hillebrandt W., Truran J. W., 1988, *A&A*, 197, L11
 Whitelock P. A. et al., 1988, *MNRAS*, 234, 5P
 Woosley S. E., Weaver T. A., 1995, *ApJS*, 101, 181
 Woosley S. E., Pinto P. A., Ensmann L., 1988, *ApJ*, 324, 466
 Woosley S. E., Heger A., Weaver T. A., 2002, *Rev. Mod. Phys.*, 74, 1015
 Yaron O., Gal-Yam A., 2012, *PASP*, 124, 668
 Zampieri L., Pastorello A., Turatto M., Cappellaro E., Benetti S., Altavilla G., Mazzali P., Hamuy M., 2003, *MNRAS*, 338, 711
 Zhang X. et al., 2022, *MNRAS*, 509, 2013
 de Vaucouleurs G., de Vaucouleurs A., Corwin Herold G. J., Buta R. J., Paturel G., Fouque P., 1991, *Third Reference Catalogue of Bright Galaxies*. Springer-Verlag, New York

APPENDIX A: NEBULAR SPECTRA OF 87A-LIKE PECULIAR SNE II

In this section, we compare the nebular-phase spectra of several SNE with those predicted by NLTE models of Dessart et al. (2021). These

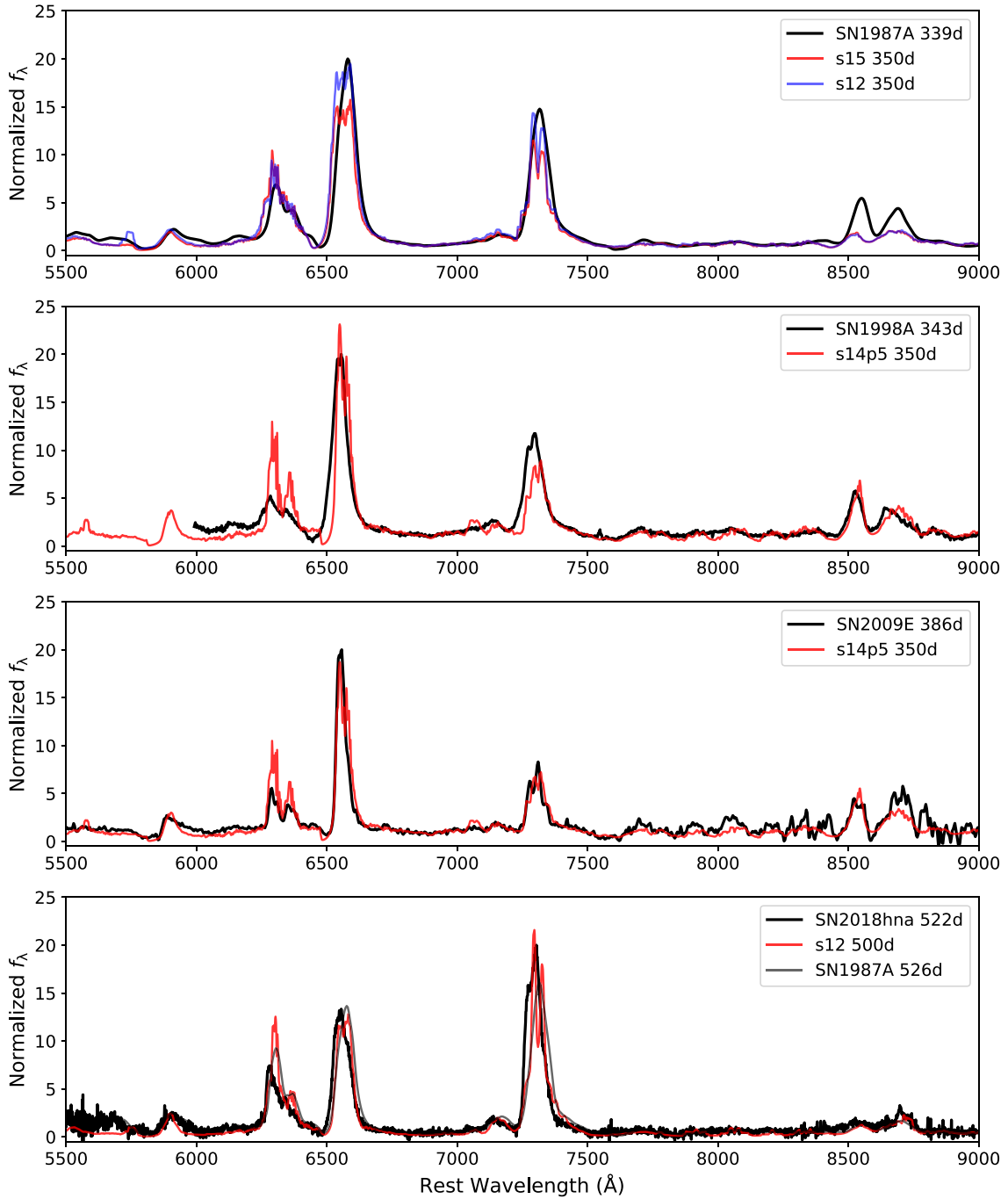


Figure A1. Nebular spectra of four 87A-like SNe compared with their best-fit models, showing the range of [O I], H α , [Ca II], and Ca II lines. For SN 2018hna, we also compare it with SN 1987A at the same phase. The spectrum flux in each panel is scaled by normalising the maximum flux of the observed spectrum to be 20.

SNe II models are extended to about 500 d after the explosion. The observed spectra of SNe 1987A, 1998A, and 2009E taken at about 1 yr after explosion and the $t \sim 522$ d spectrum of SN 2018hna are used to compare with these NLTE models in Fig. A1. For each spectrum, the model spectra are normalized to match the flux of the observed spectrum in the range 6780–7000 Å, and the model with the least squares is selected as the best fit. The initial masses of the best-fit models are 15, 14.5, 14.5, and 12 M_{\odot} for SN 1987A, SN 1998A, SN 2009E, and SN 2018hna, respectively.

Compared with model s12 at day 500, the H α , [Ca II], Ca II NIR triplet, and [O I] $\lambda\lambda 6300, 6364$ lines are of comparable strength in the $t \sim 522$ d spectrum of SN 2018hna, but the observation has weaker [O I] $\lambda\lambda 6300, 6364$. Moreover, the profile of [Ca II] doublet near 7300 Å is quite different from the model: it is a broad and flat line rather than two spikes as in the model. We caution that there may be contamination from emission of [Ni II] and [Fe II] in the observed spectrum, so this difference is hard to determine. Also, it is widely known that dust formation is common in core-collapse SNe, and dust emission will affect the line profiles of their nebular spectra. The H α

line profile shows a clear flux excess in blue and deficit in red, which is a sign of dust emission (see Appendix. B). Compared with the spectrum of the same epoch in SN 1987A, the [O I] $\lambda\lambda 6300, 6364$ line of SN 2018hna is weaker, but the [Ca II] lines are stronger, and the line profiles are also different.

The [O I] line of SN 1987A is consistent with the s15A model, but has stronger H α , [Ca II], and Ca II lines. If only the wavelength range shown in the figure is considered in fitting, the best match is the s12 model, whose initial mass is $12 M_{\odot}$, but the metal lines of the model at the blue end are significantly stronger than those in SN 1987A. The H α line of SN 1998A is consistent with the s14p5 model, but the [Ca II] lines are stronger, and the [O I] lines are much weaker than in the model. The H α line and [Ca II] lines of SN 2009E are consistent with model s14p5, while the [O I] $\lambda\lambda 6300, 6364$ line is weaker than the model, although [O I] $\lambda 5577$ is comparable to the model.

Because the models of Dessart et al. (2021) make use of pre-explosion profiles of stars with $Z = Z_{\odot}$, which differs from the environments of the observed SNe, the above fitting results do not mean that their progenitor stars have the same initial masses as the best-fit models. But the takeaway is that 87A-like SNe II are all oxygen-poor, with SN 1998A having the lowest oxygen abundance. Although the host galaxy of SN 1998A has approximately the solar metallicity (Taddia et al. 2013), the intensity of its [O I] lines is substantially lower than that of the model, which also has a relatively small initial mass ($14.5 M_{\odot}$). Note that stars of this low mass are likely to explode as RSGs rather than BSGs. Combining the analysis of oxygen mass in the SN ejecta (Section 6), the evolution mechanism of the progenitor stars of SNe 1998A, 2009E, and 2018hna may be different from that of SN 1987A.

APPENDIX B: DUST FORMATION

Dust formation is common in SNe IIP (e.g. Bevan & Barlow 2016; Niculescu-Duvaz et al. 2022; Zhang et al. 2022). Newly formed dust within the ejecta of SNe can cause a deficit in the red side of the emission lines and produce blueshifted peaks. Also, emission of CO ($\sim 2.3 \mu\text{m}$) was detected in SN 2018hna in the NIR spectrum on day 153 (Rho et al. 2019). To estimate the dust formation for SN 2018hna, we use the code DAMOCLES (Bevan & Barlow 2016; Bevan 2018) to model the H α line of SN 2018hna in its $t \approx 522$ d spectrum. DAMOCLES is a Monte Carlo line radiative transfer code which models the extent and shape of the dust-affected line profiles. We follow the method described by Bevan (2018), which applied the affine-invariant ensemble sampler for emcee to DAMOCLES.

The code has 10 free parameters, while for simplicity and saving computing resources, we vary only the dust mass and fix the

remaining nine parameters. The values of the fixed parameters and

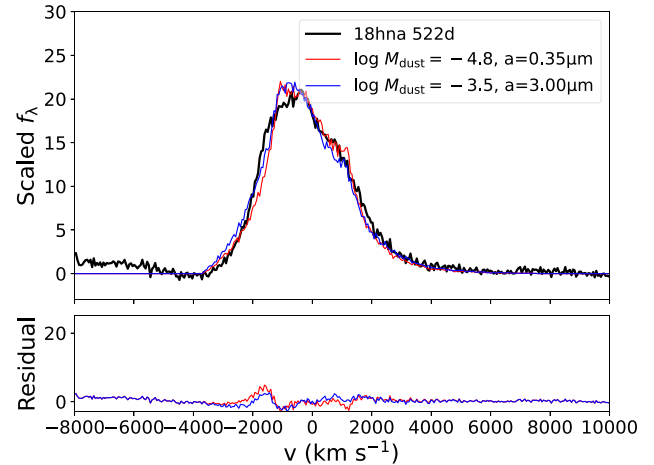


Figure B1. DAMOCLES dust model (upper) and residual (lower) for the H α line of SN 2018hna at 522 d after explosion.

dust properties are referenced from the results for SN 1987A by Bevan & Barlow (2016) as follows. We assume a smooth dust distribution without clumping. The dust and gas are coupled with the same density profile, $\rho \propto r^{-\beta}$ with $\beta = 2$. The values of V_{max} and V_{min} are measured from the observed spectrum. The dust is assumed to be 100 per cent amorphous carbon with a grain size of $a = 0.35 \mu\text{m}$. The best-fit model (see Fig. B1) shows that the total dust formed up to $t \approx 522$ d after explosion is $\log M_{\text{dust}} = -4.80^{+0.04}_{-0.09} M_{\odot}$. If the newly formed dust follows the prediction of the relationship suggested by Bevan et al. (2020), we get $\log M_{\text{dust}} \approx -3.5 M_{\odot}$, which is over one order of magnitude larger than the value we derived for SN 2018hna. If $\log M_{\text{dust}} = -3.5 M_{\odot}$ is applied, a larger dust grain size of $\sim 3 \mu\text{m}$ is required to match the observation. This may imply that the dust formed in SN 2018hna has different properties than that in SN 1987A.

APPENDIX C: OBSERVATIONAL DATA

Magnitudes of the reference stars in the field of SN 2018hna are listed in Table C1. Photometric results from the TNT images are displayed in Table C2. Magnitudes in gr -bands of ZTF are averaged by dates and listed in Table C3. The details of TNS spectra and our optical spectroscopic observations for SN 2018hna are presented in Tables C4 and C5, respectively.

Table C1. Magnitudes and 1σ uncertainties of reference stars in field of SN 2018hna.

Star No.	RA (J2000)	Dec. (J2000)	<i>B</i>	<i>V</i>	<i>g</i>	<i>r</i>	<i>i</i>
1	12h26m38s.16	+58°18'17".48	13.96(02)	13.12(08)	13.52(01)	12.96(02)	12.81(01)
2	12h26m05s.78	+58°20'33".33	16.72(03)	15.21(09)	16.04(02)	14.69(02)	14.18(02)
3	12h26m01s.30	+58°20'02".59	14.56(02)	13.34(08)	13.99(02)	12.96(03)	12.64(01)
4	12h26m28s.42	+58°15'00".04	15.29(03)	14.58(06)	14.90(01)	14.47(01)	14.32(02)
5	12h25m58s.62	+58°17'05".73	14.74(01)	13.84(09)	14.28(02)	13.66(01)	13.48(02)
6	12h26m04s.51	+58°21'39".44	16.40(01)	15.75(05)	16.03(01)	15.73(01)	15.73(03)
7	12h25m47s.17	+58°15'00".19	16.72(07)	16.01(06)	16.33(01)	15.80(02)	15.64(03)
8	12h26m00s.69	+58°18'33".11	16.83(06)	16.00(05)	16.40(02)	15.74(02)	15.51(02)
9	12h25m35s.11	+58°13'49".34	17.11(07)	16.03(09)	16.59(02)	15.72(03)	15.51(02)
10	12h25m49s.71	+58°17'06".76	17.83(06)	16.80(06)	17.33(01)	16.44(02)	16.13(03)

Table C2. *BVgri* photometric observations (mag, 1σ) of SN 2018hna from TNT.

MJD	<i>B</i>	<i>V</i>	<i>g</i>	<i>r</i>	<i>i</i>
58456.8818	15.768(023)	14.775(030)	15.198(007)	14.653(007)	14.713(012)
58459.8841	15.683(021)	14.695(028)	15.109(006)	14.565(004)	14.631(004)
58463.8584	15.583(022)	14.596(028)	15.021(008)	14.475(009)	14.551(031)
58464.8363	15.553(020)	14.575(029)	14.998(007)	14.452(006)	14.526(005)
58465.8534	15.532(022)	14.550(029)	14.967(015)	14.422(017)	14.489(010)
58466.8849	15.517(021)	14.530(028)	14.949(008)	14.405(010)	14.479(005)
58468.9026	15.518(073)	14.496(042)	14.900(023)	14.364(030)	14.437(038)
58469.8456	15.438(030)	14.471(048)	14.893(017)	14.353(020)	14.419(013)
58476.8029	15.305(022)	14.356(028)	14.743(022)	14.228(008)	14.308(007)
58477.7920	15.308(024)	14.351(030)	14.741(008)	14.230(011)	14.299(013)
58478.8260	15.306(028)	14.349(029)	14.728(008)	14.237(016)	14.291(009)
58479.7832	15.311(030)	14.329(028)	14.735(008)	14.202(007)	14.263(006)
58480.7888	15.255(021)	14.318(029)	14.721(009)	14.182(006)	14.258(005)
58481.8202	15.243(022)	14.292(030)	14.699(010)	14.170(013)	...
58482.8812	15.225(084)	14.281(100)	14.701(008)	14.144(032)	...
58484.8716	15.201(024)	14.253(030)	14.660(010)	14.135(014)	14.199(035)
58486.8623	15.157(026)	14.241(029)	14.640(005)	14.107(004)	14.191(016)
58487.8341	15.172(020)	14.234(028)	14.632(008)	14.104(005)	14.184(016)
58489.8028	15.150(021)	14.219(031)	14.610(009)	14.081(006)	14.148(009)
58490.8340	15.148(021)	14.206(029)	14.580(006)	14.075(006)	14.138(014)
58491.9155	15.130(039)	14.207(034)	14.602(012)	14.071(009)	14.126(028)
58495.9295	14.601(039)	14.117(045)	...
58498.8507	15.134(022)	14.186(028)	14.582(005)	14.031(005)	14.098(018)
58499.8604	15.143(021)	14.188(031)	14.598(009)	14.047(021)	14.094(016)
58500.8375	15.168(031)	14.195(029)	14.615(025)	14.049(017)	14.099(016)
58503.8620	15.224(031)	14.242(029)	14.640(011)	14.063(006)	14.118(007)
58504.8879	15.247(025)	14.250(031)	14.684(011)	14.080(008)	14.121(017)
58506.8683	15.360(045)	14.308(038)	14.780(039)	14.131(036)	14.160(039)
58507.8622	15.373(031)	14.316(044)	14.781(010)	14.130(013)	14.146(011)
58515.8312	16.055(022)	14.826(028)	15.375(010)	14.538(007)	14.497(004)
58530.8982	16.855(026)	15.530(029)	16.132(011)	15.149(011)	15.047(015)
58533.8840	16.935(067)	15.601(039)	16.172(021)	15.199(013)	15.090(041)
58534.7725	16.913(048)	15.594(034)	16.167(017)	15.205(025)	15.102(024)
58537.6673	17.184(033)	15.624(030)	16.192(012)	15.199(007)	15.120(013)
58538.7867	16.954(035)	15.671(036)	16.222(024)	15.255(025)	15.133(019)
58543.6943	16.967(026)
58545.6754	17.011(046)	15.735(038)	16.297(008)	15.291(010)	15.224(019)
58554.6898	17.167(027)	15.853(030)	16.437(011)	15.410(012)	15.331(019)
58559.7581	17.088(132)	15.899(050)	...	15.459(026)	...
58560.5376	17.132(131)	15.938(039)	16.410(045)
58566.6336	17.259(030)	15.973(032)	16.549(020)	15.499(017)	15.432(018)
58575.5722	17.350(025)	16.095(029)	16.653(010)	15.584(009)	15.526(011)
58576.5732	17.336(029)	16.102(030)	16.657(011)	15.593(011)	15.542(010)
58577.6453	17.398(032)	16.135(030)	16.679(011)	15.608(006)	15.556(006)
58580.6479	17.451(058)	16.263(060)	16.719(034)	15.644(036)	15.656(057)
58589.6703	17.555(157)	16.229(076)	16.874(079)	15.726(026)	15.698(031)
58590.7650	16.652(132)	15.558(103)	15.687(074)
58599.6243	17.665(025)
58603.6161	17.659(030)	16.429(029)	16.970(010)	15.822(011)	15.789(017)
58604.7262	17.684(027)	16.454(030)	16.978(008)	15.838(008)	15.796(017)
58608.6191	17.749(041)	16.511(030)	17.049(009)	15.874(012)	15.841(011)
58609.7037	17.750(038)	16.535(030)	17.067(010)	15.902(009)	15.876(017)
58623.6030	17.911(045)	16.694(032)	17.219(015)	16.012(012)	15.999(012)
58631.6280	17.970(038)	16.784(039)	17.294(043)
58634.5618	17.998(034)	16.818(029)	17.337(023)	16.114(011)	16.096(017)
58645.6379	18.074(080)	16.934(050)	17.425(037)	16.183(013)	16.191(018)
58649.5714	18.111(225)	17.082(079)	17.549(085)	16.233(032)	16.277(036)
58663.6125	18.208(040)	17.146(037)	17.627(025)

Table C3. Photometric magnitudes and uncertainties in *gr*-bands of SN 2018hna from ZTF.

MJD	<i>g</i>	<i>r</i>	MJD	<i>g</i>	<i>r</i>	MJD	<i>g</i>	<i>r</i>
58423.512	16.409(004)	15.794(018)	58633.235	17.327(040)	16.015(012)	58827.443	...	18.258(057)
58426.496	16.391(090)	15.765(041)	58634.229	17.350(001)	...	58828.494	19.211(001)	18.349(001)
58429.518	16.320(054)	15.623(030)	58636.270	17.356(041)	...	58830.508	19.248(059)	18.368(001)
58432.513	16.184(032)	15.485(016)	58637.214	17.368(001)	16.074(001)	58831.502	19.226(001)	18.439(001)
58440.505	15.938(149)	15.224(011)	58639.230	17.384(040)	16.107(006)	58833.515	19.306(180)	18.399(052)
58443.470	15.843(001)	15.107(008)	58640.216	17.423(001)	16.114(001)	58835.475	...	18.395(001)
58447.476	...	14.934(010)	58642.217	17.412(021)	16.103(007)	58836.531	19.288(046)	18.443(025)
58450.496	15.461(025)	...	58643.221	17.424(001)	16.121(001)	58838.494	18.996(001)	18.497(001)
58461.485	15.107(053)	...	58645.223	17.476(022)	...	58846.543	19.403(025)	18.629(033)
58464.501	15.046(022)	...	58646.209	17.478(020)	16.180(017)	58849.476	19.467(015)	18.646(001)
58471.532	14.871(028)	14.292(045)	58648.195	17.481(025)	16.159(003)	58851.537	19.428(010)	...
58474.490	...	14.197(001)	58649.210	17.505(036)	16.171(016)	58852.541	19.490(029)	18.685(007)
58476.540	14.859(001)	14.173(001)	58651.223	17.512(058)	16.207(009)	58855.531	19.443(026)	18.740(040)
58480.515	14.745(038)	...	58652.279	...	16.214(040)	58859.469	19.461(036)	18.869(040)
58486.521	14.656(024)	14.060(025)	58654.244	17.523(048)	16.217(001)	58860.313	...	18.728(106)
58491.522	14.627(039)	14.012(009)	58655.210	17.552(011)	16.234(009)	58861.503	19.418(001)	18.695(001)
58494.505	14.609(029)	...	58657.199	17.590(001)	...	58862.431	19.496(122)	18.887(040)
58502.501	14.611(010)	13.986(023)	58658.200	17.586(015)	...	58864.332	...	18.906(001)
58505.492	14.710(017)	14.019(002)	58660.186	17.644(001)	...	58866.466	19.683(001)	18.952(001)
58508.513	14.838(027)	14.098(005)	58661.213	17.593(023)	16.274(008)	58867.452	19.641(030)	18.915(026)
58511.427	15.056(071)	14.219(010)	58665.232	17.603(001)	16.364(001)	58871.482	19.641(031)	18.988(071)
58514.444	15.226(042)	14.381(011)	58667.212	17.687(023)	16.340(001)	58872.429	19.701(008)	...
58522.501	15.870(049)	14.871(005)	58668.192	17.668(001)	16.385(001)	58873.390	19.678(071)	19.005(024)
58526.484	16.043(024)	14.994(001)	58670.211	17.687(031)	16.381(014)	58874.346	19.643(001)	19.185(001)
58534.342	16.244(276)	15.118(009)	58671.200	...	16.324(001)	58875.459	19.626(112)	19.141(086)
58538.317	16.258(069)	15.208(018)	58673.191	17.732(045)	16.408(010)	58876.378	19.753(056)	19.079(025)
58540.268	...	15.184(001)	58674.209	17.728(001)	16.423(001)	58877.466	19.747(054)	19.103(032)
58543.316	16.275(047)	15.220(024)	58676.192	17.743(051)	16.436(004)	58878.414	19.653(056)	19.087(044)
58546.271	16.315(016)	...	58677.190	17.781(001)	16.463(001)	58879.384	19.700(168)	19.138(070)
58556.280	16.435(026)	15.401(001)	58679.200	17.744(001)	16.448(001)	58880.486	19.738(075)	19.137(025)
58558.214	...	15.326(001)	58680.214	17.768(001)	16.468(001)	58881.424	19.765(077)	19.111(037)
58559.304	16.513(054)	15.389(013)	58682.247	...	16.500(001)	58883.490	19.709(029)	19.205(047)
58562.317	16.572(016)	15.419(001)	58683.224	17.827(046)	16.506(008)	58884.479	19.760(109)	19.146(071)
58567.306	16.510(001)	15.456(011)	58684.245	17.936(001)	16.547(001)	58885.439	19.859(049)	19.204(051)
58572.296	16.663(033)	15.492(010)	58686.197	17.839(015)	...	58886.451	19.685(081)	19.217(048)
58574.238	...	15.387(001)	58688.201	17.895(001)	...	58887.378	19.504(001)	19.195(096)
58575.306	16.672(032)	15.534(012)	58689.692	17.890(012)	16.482(001)	58888.441	...	19.317(118)
58580.283	16.744(022)	15.571(006)	58690.176	...	16.581(001)	58890.432	...	19.197(049)
58583.269	...	15.589(001)	58691.221	17.954(001)	...	58891.427	19.947(001)	19.226(008)
58584.288	16.767(002)	15.586(010)	58692.197	17.910(030)	16.609(001)	58892.346	19.878(001)	19.297(017)
58586.223	16.804(041)	15.624(005)	58693.248	17.895(020)	...	58893.372	19.883(093)	19.353(066)
58587.300	16.814(043)	15.630(005)	58694.198	17.922(001)	16.606(001)	58894.414	20.060(111)	19.305(041)
58589.245	16.844(013)	15.693(043)	58695.164	17.954(049)	...	58895.397	19.973(014)	19.342(105)
58590.765	16.652(132)	...	58701.163	...	16.682(001)	58898.395	19.985(050)	19.420(040)
58591.298	16.814(009)	15.699(040)	58705.204	18.020(001)	16.726(001)	58899.386	19.940(149)	19.433(025)
58592.222	16.907(033)	15.670(036)	58706.205	18.049(001)	16.750(001)	58900.366	19.963(042)	19.388(081)
58593.287	...	15.658(001)	58707.203	18.106(001)	16.747(001)	58901.397	...	19.439(039)
58594.279	16.860(033)	15.693(007)	58709.190	...	16.787(001)	58903.377	20.117(054)	19.439(053)
58596.211	16.958(009)	...	58716.154	18.164(001)	...	58904.446	19.988(054)	19.433(070)
58597.302	16.925(039)	15.709(002)	58720.159	18.171(008)	...	58905.257	20.053(115)	19.466(001)
58599.183	16.970(025)	15.747(001)	58726.151	18.240(001)	16.971(001)	58906.385	20.042(064)	19.502(072)
58600.211	16.929(005)	...	58776.512	...	17.582(011)	58908.393	19.999(076)	19.622(050)
58602.250	17.119(001)	15.789(001)	58779.515	18.670(001)	...	58911.438	19.957(043)	19.550(003)
58606.321	17.014(013)	15.798(017)	58785.509	...	17.728(024)	58912.424	20.082(044)	19.602(041)
58608.261	...	15.783(001)	58786.529	18.842(099)	...	58913.383	20.037(120)	19.603(069)
58609.205	17.054(009)	...	58789.512	18.820(041)	...	58914.413	20.312(001)	19.629(092)
58612.221	17.110(040)	15.844(013)	58792.523	18.871(035)	17.850(018)	58915.391	...	19.773(041)
58616.209	17.151(037)	15.884(013)	58799.492	...	17.913(045)	58936.349	20.607(072)	20.010(073)
58618.205	...	15.882(001)	58802.549	18.910(082)	...	58954.275	20.697(209)	20.357(131)
58619.224	17.192(041)	15.905(007)	58804.519	19.055(001)	18.023(001)	58956.290	...	20.333(001)
58622.166	17.237(001)	...	58805.532	19.016(060)	...	58962.263	20.767(001)	20.334(085)
58628.267	17.273(029)	15.984(001)	58812.493	19.145(001)	18.121(026)

Table C4. Details of TNS spectra of SN 2018hna.

ID	UT	MJD	Telescope (instrument)	Exp. time (s)	Observer(s)
2933	2018/10/24.80	58415.80	Kanata / HOWPol	900	K. Takagi, T. Nakaoka, M. Kawabata
2930	2018/10/26.72	58417.72	ALPY	3006	R. Leadbeater
2974	2018/11/02.53	58424.53	P60/SEDM	1600	ZTF

Table C5. Spectroscopic observations of SN 2018hna.

UT	MJD	Telescope	Instrument	Exp. time (s)
2018/12/04.89	58456.89	BAO 2.16 m	BFOSC	3300
2018/12/08.88	58460.88	BAO 2.16 m	BFOSC	3300
2018/12/09.50	58462.50	APO 3.5 m	DIS	2400
2018/12/11.87	58463.87	BAO 2.16 m	BFOSC	3300
2018/12/14.87	58466.87	BAO 2.16 m	BFOSC	3300
2018/12/16.88	58468.88	BAO 2.16 m	BFOSC	3000
2018/12/22.88	58474.88	BAO 2.16 m	BFOSC	3300
2019/01/01.90	58484.90	BAO 2.16 m	BFOSC	2400
2019/01/06.90	58489.90	BAO 2.16 m	BFOSC	2400
2019/01/25.91	58508.91	LJO 2.4-m	YFOSC	1800
2019/01/29.80	58512.80	BAO 2.16 m	BFOSC	3000
2019/01/31.84	58514.84	BAO 2.16 m	BFOSC	3000
2019/02/11.66	58525.66	BAO 2.16 m	BFOSC	3000
2019/02/15.70	58529.70	LJO 2.4-m	YFOSC	1000
2019/02/20.75	58534.75	LJO 2.4-m	YFOSC	1000
2019/02/23.84	58554.84	BAO 2.16 m	BFOSC	3000
2019/03/12.85	58565.85	BAO 2.16 m	BFOSC	3000
2019/03/26.77	58568.77	BAO 2.16 m	BFOSC	3300
2019/04/02.75	58575.75	LJO 2.4-m	YFOSC	1500
2019/05/06.61	58609.61	BAO 2.16 m	BFOSC	2700
2019/06/11.55	58645.55	BAO 2.16 m	BFOSC	2700
2019/06/23.54	58657.54	BAO 2.16 m	BFOSC	2700
2020/03/24.63	58932.63	Keck-I 10 m	LRIS	610

This paper has been typeset from a \LaTeX file prepared by the author.